

Applications of MXene-Based Single-Atom Catalysts

Xue Bai and Jingqi Guan*

Single-atom catalysts (SACs) consist of isolated metal sites on the support through stable coordination bond, which usually have high catalytic activity and selectivity. With large surface area and electron tunability, metallic carbides, nitrides, or carbonic nitrides (MXenes) are suitable carriers for supporting isolated single-metal atoms. The abundant surface-functional groups and vacancy defects on MXenes are the ideal anchoring sites for isolated metal atoms. Herein, the advanced synthesis and characterization methods for MXene-based SACs are first introduced. Three strategies (adsorption at functional groups, anchoring at metal vacancies, and anchoring at surface terminating group vacancies) appear to be feasible in ensuring the non-aggregation of single-metal atoms, which are attributed to the strong bonding between the single-metal atoms and the carrier. The applications of MXene-based SACs in electrocatalysis (including hydrogen evolution reaction, oxygen evolution reaction, oxygen reduction reaction, carbon dioxide reduction reaction, and nitrogen reduction reaction), energy storage (including Li-ion batteries, metal–air batteries, and supercapacitors), and sensors (including gas sensors and biological sensors) are fundamentally reviewed. Finally, own insight on the current challenges and prospects of MXene-based SACs is presented.

of the active site, the catalytic performance can be significantly improved. Thus, design and synthesis of catalysts on atomic scale is an efficient strategy to improve catalytic activity.

In 2011, Zhang et al. prepared atomically dispersed Pt species and proposed the concept of single-atom (SA) catalyst for the first time, defining single-atom catalysts (SACs) as a supported catalyst in which metal species are dispersed in the form of isolated atoms.^[1] Compared with traditional catalysts, SACs have an atomic utilization efficiency of 100%, and can achieve high catalytic performance under low metal load, which greatly reduces the production cost.^[2] Shi et al. loaded only 4.1 wt% Pt SAs on the surface of MoSe₂, showing excellent alkaline electrocatalytic hydrogen evolution performance.^[3] In addition, SACs have the properties of reusability and controllable structure, which combine the advantages of homogeneous and heterogeneous catalysis.^[4,5] Usually, single-metal sites have uniform and adjustable coordination structures,


showing the superiority of catalyzing specified reactions and improving product selectivity. By changing the activation temperature, Ren et al. synthesized Pt SAs with different electronic environment and oxidation state on Fe₂O₃ in a controllable manner.^[6] Moreover, Pd SAs with different coordination are synthesized by replacing different organic ligands, and the Pd@POL-1 coordinated with organic phosphine showed high catalytic selectivity for the hydrosilylation reaction of internal alkyne.^[7]

Due to the high cohesive energy, individual metal atoms tend to aggregate to form nanoclusters.^[8] To obtain stable and highly dispersed metal atoms, it is usually necessary to anchor the isolated metal atoms onto a substrate, where strong charge transfer would occur through the bonding of the metal atoms to the reactive sites on the substrate. Metal oxide, metal–organic framework, molybdenum disulfide, graphene, and so on are common carriers that can be used to fix metal atoms.^[9–13] Among them, 2D materials show good application prospects due to large specific surface area.^[14,15] As a new type of 2D materials, metallic carbides, nitrides, or carbonic nitrides (MXenes), with the general structure of M_{n+1}X_nT_x, where M is transition metal (TM), X is carbon/nitrogen element, T is the surface terminating group (–O, –OH, –F, etc.), and *n* = 1, 2, 3, or 4, are ideal substrate candidates for anchoring SA sites due to high surface energy, adjustable electronic structure, and uniform atomic arrangement. The surface-functional groups in MXenes are electronegative, which can adsorb metal cations and are conducive to

1. Introduction

Catalytic science, including heterogeneous catalysis, homogeneous catalysis, and enzyme catalysis, is involved in various fields of production and life, including energy, pharmaceuticals, environmental protection and so on. Thereinto, heterogeneous catalysis, which is usually driven by metal-based catalysts, effectively reduces production costs due to its easy recovery nature and thus plays a dominant role in industrial production. However, the distribution of active sites in heterogeneous catalysts is uncontrollable, and it is difficult to utilize the structure–activity relationship to adjust the catalyst performance. Through reducing the size of the nonmetallic catalyst and increasing the exposure

X. Bai, J. Guan
Institute of Physical Chemistry
College of Chemistry
Jilin University
2519 Jiefang Road, Changchun 130021, P. R. China
E-mail: guanjq@jlu.edu.cn

 The ORCID identification number(s) for the author(s) of this article can be found under <https://doi.org/10.1002/ssstr.202200354>.

© 2023 The Authors. Small Structures published by Wiley-VCH GmbH. This is an open access article under the terms of the Creative Commons Attribution License, which permits use, distribution and reproduction in any medium, provided the original work is properly cited.

DOI: 10.1002/ssstr.202200354

further reduction and anchoring. In addition, the preparation process of MXenes usually requires the addition of etching agents to selectively remove unwanted metal atoms, but some metal atoms inside the MXene lattice will inevitably be etched away, resulting in metal defect sites. The defect sites of unsaturated coordination have certain reducibility, where the adsorption and reduction of metal cations can be simultaneously achieved by one step method.

MXene-based SACs have been widely studied and applied in various fields. In this review, we first discuss the properties and advantages of MXenes as carriers to load single-metal atoms, and summarize the existing characterization methods of single-metal sites. Second, the theoretical basis, synthesis methods, and strategies for the stabilization of single-atomic sites on MXenes are systematically summarized. Adsorption on surface-functional groups and filling in M and T vacancies are the main anchoring strategies. Then, the applications of MXene-based SACs in the fields of electrocatalysis, energy storage, and sensor are introduced. Finally, the prospect of MXene-based SACs is proposed.

2. The Sites of MXenes for Anchoring Isolated Metal Atoms

2.1. Synthesis of MXenes

In 2011, the first MXene Ti_3C_2 was synthesized by Naguib et al. by selectively removing Al atoms from Ti_3AlC_2 , which was defined as MAX (A is Al element).^[16] Due to the weak binding energy of Al in MAX, it exhibited higher reactivity than Ti species. After treatment in 50% hydrogen fluoride (HF) solution, the Al atoms combined with F to form AlF_3 and volatilized from the precursor Ti_3AlC_2 , retaining MXene Ti_3C_2 . Subsequently, this top-down strategy was popularized and was the dominant method for MXene synthesis (Figure 1a). Ti- and Mo-based MAX are commonly used precursors that can be easily purchased, while other specific MAX are usually synthesized in the laboratory. By mixing a molar ratio of TM, Al, and graphite,

and annealing at high temperature, MAX with target metal can be obtained, including bimetallic MAX. For example, Nb_4AlC_3 , with multiple atomic layers, was synthesized by treating Nb, Al, and C mixtures under high temperature and pressure.^[17] In addition, MXenes can be also obtained by the removal of the A element. The commonly used etching agent is HF and the concentration and temperature required for the synthesis of different MXenes are different. Jiang et al. synthesized Ti_3C_2 and V_2C quantum dots with an average size of 4.5 nm under different conditions, at 25 °C with 40% HF for V_2AlC and at 50 °C with 48% HF for V_2AlC .^[18] The HCl/LiF solutions are also used in the etching process, which are more controlled, mild, and environmentally friendly than HF. In addition, Li^+ can enter the MXene interlayer during the etching process to obtain MXene with a few layers or single layer. Moreover, MXenes can be synthesized by the stripping of multilayer MXenes. Multilayer MXene obtained by F^- etching is washed with deionized water and ultrasonic until the pH is neutral. During this process, H_2O molecules would enter the interlayer and reduce the tendency of MXene aggregation. To avoid the unsatisfactory small layer structure caused by prolonged ultrasound, additional intercalators, such as metal cations, organic molecules, and so on, are added to widen the layer spacing and accelerate stripping and stratification of MXenes. Due to the high corrosion and danger of fluorine-containing reagents, fluorine-free etching has been widely developed, including high-temperature alkali treatment, molten salts etching, electric etching, and so on.^[19–21] In addition, MXene with chlorine-functional groups would be obtained through by etching MAX with molten chloride salts.^[22]

In addition to MXenes with monometal and bimetals, high-entropy MXenes with more than three TMs have been designed. Leong et al. calculated the thermostatically stable configurations of TiVNbMoC_3 and TiVCrMoC_3 , and found that the metals showed obvious preferential occupation at high temperatures, with Cr most inclined to the outer layer, followed by Mo.^[23] In addition, the metals in high-entropy MAX precursor were in a solid solution state above 1873 K, while Nb and V atoms showed significant separation in the inner layer below 928 K.

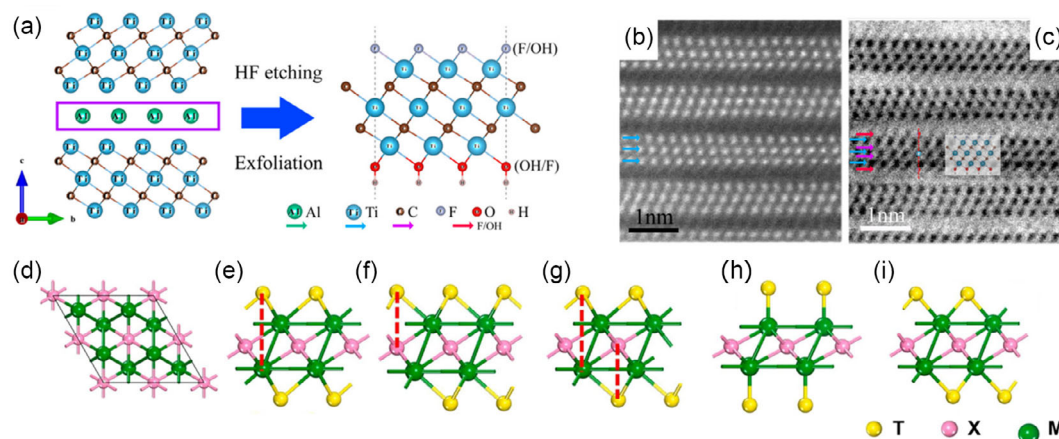


Figure 1. a) Synthesis and structure of $\text{Ti}_3\text{C}_2\text{T}_x$. b) High-angle annular dark-field (HAADF) and c) Annular bright-field images of $\text{Ti}_3\text{C}_2\text{T}_x$ observed along the a/b axis. Reproduced with permission.^[120] Copyright 2015, American Chemical Society. d) Top view of 2D M_2X (X = C or N). Side views of configuration of e) fcc, f) hcp, g) fcc + hcp, h) top, and i) bridge. Reproduced with permission.^[121] Copyright 2018, Elsevier.

2.2. Abundant Sites for Anchoring Isolated Metal Atoms

MXene, with a hexagonal lattice structure, is composed of M metal layer and carbon/nitrogen atom layer arranged alternately, where carbon and nitrogen atoms are in the inner layer (Figure 1d–i). Due to the high surface energy, metals exposed in the outer layer will usually bond with functional groups such as F, O, and OH, while coordinating with three carbon or nitrogen in the inner layer to form a six-coordination structure. There are two main coordination configurations of surface-functional groups, face center cubic (fcc) and hexagonal close packed (hcp), and the optimal coordination configurations are different for different TMs.^[24] The electronegative surface-functional groups are ideal sites for fixing isolated metal atoms, which can easily adsorb metal cations. Theoretical calculations showed that the stability of different single atoms at the terminal is different.^[25] The stability of SACs is often associated with the intrinsic properties of metal–support interaction, including kinetic stability and thermodynamic stability.^[26] When the formation energy of an isolated metal atom on the carrier is lower than that of a nanoparticle, the formation of SA site is thermodynamic favorable. Under certain conditions, such as the addition of a small number of metal precursors, SA sites are preferentially generated, which can remain dispersed state due to the presence of a high aggregation barrier. Under the guidance of theoretical calculations, it is meaningful to design and synthesize the advantageous terminal. Furthermore, the type and proportion of surface terminals are related to the method of MXene synthesis, and the oxygen end is the more stable end group due to the strong M–O bond.^[27] MXene obtained by strong alkali etching achieved 100%–O/–OH coverage.^[28] However, high concentration of HF would increase the content of F on the surface, and high temperature can also remove part of the O-functional group, correspondingly increasing the ratio of F.^[29]

In addition, the unanticipated lattice defects of MXene are advantageous for the anchoring of single atoms.^[30–32] In the process of MXene synthesis, in addition to Al atoms, some metal atoms will be taken away by strong acids, leaving highly active metal vacancies on the surface of MXene. Due to unsaturated coordination structure of defect sites, the adsorbed metal ions are reduced in situ without the need for additional high temperature or reducing atmosphere. According to different distribution of metals, bimetallic M_1, M_2 -MXene can be divided into ordered MXene and solid solution MXene, which both exhibit more favorable properties for loaded metal atoms. Selective etching of metals M_1 from M_1, M_2 -MXene results in uniformly dispersed vacancies for filling the target single atoms. In addition, by taking the target single atom as metal M_1 and adjusting the ratio of metal M_1 and M_2 , atomically dispersed M_1 single atom can be directly obtained.

3. Strategies of Anchoring Isolated Metal Atoms onto MXenes

The high tendency of polymerization of single atoms on the surface of the MXene is a major challenge in the synthesis of SACs. Therefore, uniform dispersion and stability of single atoms in the catalytic process is the key to improve the utilization rate of single-atom active sites. The T-functional groups of MXene

have negative charge and can be designed as coordination sites to facilitate the adsorption and fixation of metal atoms, which is the preferred single-atom synthesis strategy. Another efficient strategy is immobilizing metal atoms using defect sites to limit atomic migration. The presence of natural M and T vacancies within the MXene structure leads to the formation of unsaturated sites, which are conducive to the formation of isolated atoms. Recent synthesis methods of MXene-based SACs are summarized in Table 1.

3.1. Adsorption on the Surface

3.1.1. Theoretical Basis

Fixation of single atoms on the surface of MXene requires specific adsorption sites. For primitive MXene, the adsorption of single atoms mainly occurs at four possible sites: top site (T), two different hollow sites fcc and hcp, and bridge sites (B), where the sites of hcp and fcc are the preferred adsorption sites (Figure 2a,b). Theoretical calculations displayed that the TM atoms were more easily adsorbed on the surface of Ti_3C_2 than graphene, with adsorption energy between -1.05 and -7.98 eV (Figure 2c).^[33] Furthermore, the increase of atomic number of TM led to the d electron center away from the Fermi level, resulting in the weakened adsorption. Moreover, Oschinski et al. studied the aggregation trend of TMs on M_2C by calculating diffusion energy.^[34] The cohesive energy of Zn was greater than 0 on the surface of all M_2C , suggesting that Zn single atom was stable on MXene surface. However, V, Cr, Mn, Fe and Co exhibited unfavorable aggregation trend on M_2C . In addition to atomically dispersed atoms on MXene surface, the charge (partial oxidation or partial reduction) state can be controlled. Nevertheless, the adsorption model of TM on MXene with functional groups (O, OH, F) should be constructed because MXene is easy to be oxidized. The adsorption sites were basically consistent with those of MXene without functional groups, top, hcp, fcc, and bridge. With the low tendency to form clusters and high diffusion barrier, Sc and Ti were the viable to form single-atom sites on M_2CO_2 .^[35]

3.1.2. Synthesis Method

MXene is primarily synthesized by fluoride ion etching, and there are F- or O-functional groups on the surface rather than bare MXene. Negatively charged functional groups are the structural basis for the adsorption of individual metal atoms on MXene. Usually, single-metal atoms on the surface of MXene are synthesized by electrostatic adsorption and in situ reduction in two steps. First, the metal cations are adsorbed on the negatively charged functional groups on the surface of MXene to form ionic bonds driven by electrostatic attraction. Subsequently, the metal cations are reduced and fixed on the MXene to form covalent bonds such as M–O/F by adding reducing agents or annealing at high temperatures. In the presence of $NaBH_4$, Co^{2+} ions are bonded to O on MXene under the drive of electrostatic attraction (Figure 3a).^[36] The successful synthesis of Co single atoms, which are coordinated with O and C, making the accumulation degree of $Ti_3C_2T_x$ significantly reduced. The addition of $NaBH_4$ avoided the excessive oxidation of MXene and facilitated the

Table 1. A summary of recently reported methods for fabrication of MXene-based SACs.

Synthetic strategies	SACs	Metal content	Methods	Applications	References
Adsorption on the surface	Co-Ti ₃ C ₂ T _x	2.4 wt%	Electrostatic adsorption	CO ₂ RR	[36]
	Ru SA _s /Ti ₃ C ₂ O	0.43 wt%	Electrostatic adsorption	NRR	[37]
	V ₂ C@Co	8.98 wt%	Electrostatic adsorption	Li-ion batteries	[56]
	Rh SA/Ti ₃ C ₂ O _x	0.17 wt%	Annealing (Ar ₂)	HER	[38]
	Ir/Mo ₂ TiC ₂ T _x	1 wt%	Annealing (H ₂)	HER	[39]
	SA-Cu-MXene	1.0 wt%	Alloying	CO ₂ RR	[40]
	Zn/V ₃ CrC ₃ T _x	–	Alloying	Zn-ion supercapacitors	[57]
	Pt SA-PNPM	2.32 wt%	High-temperature pyrolysis	HER	[55]
	Ir _{SA} -2NS-Ti ₃ C ₂ T _x	2.5 wt%	High-temperature pyrolysis	HER	[58]
	Sb SQ@MA	60.3 wt%	Hydrothermal method	K-ion batteries	[59]
Anchoring at the M vacancies	Fe-SA/Mo ₂ TiC ₂ T _x	1.8 wt%	Electric-reduction method	Peroxymonosulfate activation	[63]
	Pt ₁ /Ti _{3-x} C ₂ T _y	0.2 wt%	Self-reduction method	Functionalization of CO ₂	[42]
	Pt-V ₂ CT _x	0.88 wt%	Self-reduction method	HER	[43]
	Ni SACs/Ti ₃ C ₂ T _x	2.93 wt%	Self-reduction method	Hydrazine oxidation reaction	[44]
	Mo ₂ CT _x :Co	0.04 wt%	Alloying	HER	[46]
Anchoring at the T vacancies	Mo ₂ CT _x :Fe	0.42 wt%	Alloying	ORR	[47]
	Co@V ₂ CT _x	1.58 wt%	Photochemical reduction method	OER/HER	[51]
	Co@Nb ₂ CT _x	1.63 wt%	Photochemical reduction method	OER/HER	[51]
	Co@Ti ₃ C ₂ T _x	1.61 wt%	Photochemical reduction method	OER/HER	[51]
	Ti ₃ C ₂ T _x -Pt _{SA}	0.84 wt%	Thermal-reaction method	HER	[52]
	Ru _{SA} -N-S-Ti ₃ C ₂ T _x	1.2 wt%	Thermal-reaction method	HER	[53]
	Cu SA/Ti ₃ C ₂ T _x	0.2 wt%	Assisted reduction method	CO reduction reaction	[50]

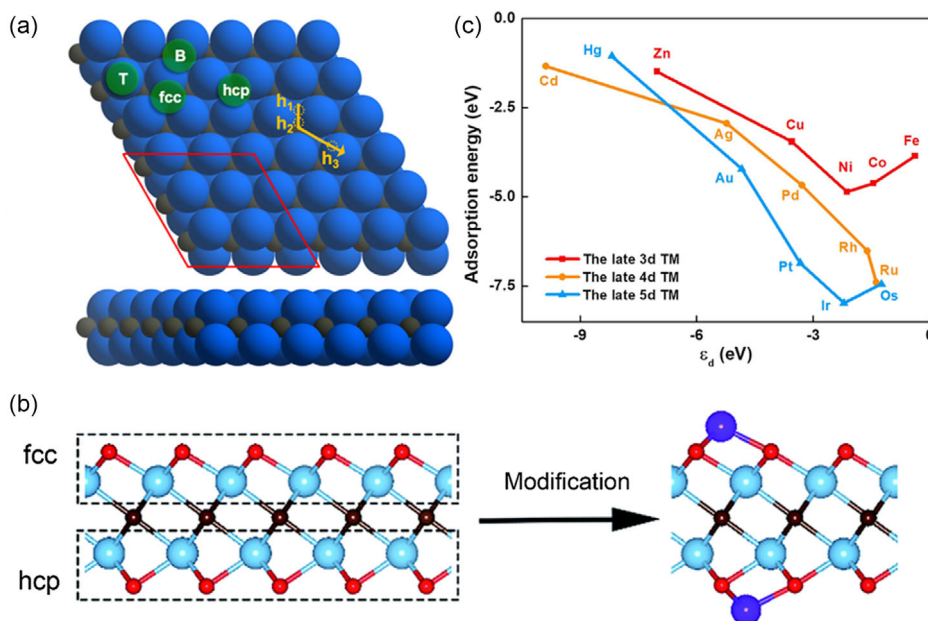


Figure 2. a) MXene structure of M₂C and the sites for anchoring single-metal atoms. Reproduced with permission.^[34] Copyright 2021, American Chemical Society. b) Adsorption model of transition metal (TM) on M₂C. Reproduced with permission.^[122] Copyright 2018, The Royal Society of Chemistry. c) The relationship between adsorption energy and the d-electron center of TM. Reproduced with permission.^[33] Copyright 2018, Elsevier.

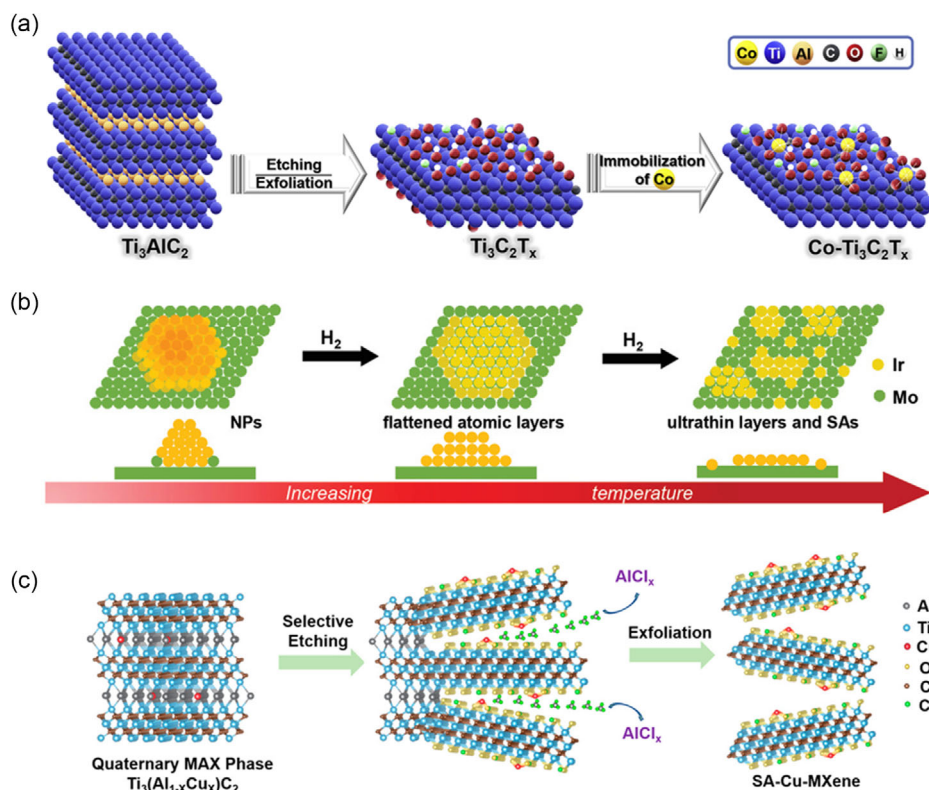


Figure 3. a) Synthetic process of Co–Ti₃C₂T_x single-atom catalysts (SAC). Reproduced under the terms of CC-BY license.^[36] Copyright 2021, The Author(s), published by Elsevier. b) The conversion scheme of Ir from nanoparticles to flattened layer and then to ultrathin layer on Mo₂TiC₂T_x. Reproduced with permission.^[39] Copyright 2022, Wiley-VCH GmbH. c) The fabrication of single atom (SA)–Cu–MXene via selective etching quaternary MAX. Reproduced with permission.^[40] Copyright 2021, American Chemical Society.

reduction of metal ions. The Ru³⁺ ions were adsorbed on oxygen end groups and reduced to Ru atoms by adding reducing tannic acid.^[37] The tannic acid was beneficial to the synthesis of Ru SAs with low load (0.43 wt%), while the corresponding Ru SAs synthesized with NaBH₄ contained 2.14 wt% Ru and Ru nanoparticles.

High-temperature annealing facilitates the formation of individual atoms from bulk metals. Peng et al. annealed Rh³⁺/Ti₃C₂O_x in an argon atmosphere to obtain Rh SA/Ti₃C₂O_x, in which 0.17 wt% Rh was uniformly dispersed on the surface of MXene.^[38] At high temperature, the structure of Ti₃C₂O_x nanosheet was not damaged, and it has a thickness of 2 nm, a transverse size of hundreds of nanometers, and a high specific surface area of 441.81 m² g⁻¹. Annealing in hydrogen atmosphere can induce the morphologic transformation of Ir species on Mo-based MXene from nanoparticles to single atoms with the increase of annealing temperature (Figure 3b).^[39] At 650 °C, Ir species exhibited octahedral nanoparticles with an average diameter of 3.5 nm, and the Ir atomic layer would be formed when continuing to heat up to 750 °C. Further, single-Ir-atoms-dominated Ir species were formed on the surface of MXene after annealing at 850 °C. There are strong metal–carrier interactions between Ir and Mo. Owing to the easy sublimation of AlCl₃, Zhao et al. selectively etched Al from the quaternary MAX phase Ti₃(Al_{1-x}Cu_x)C₂, which contained a mixed A layer, and obtained Cu single atoms on the surface of MXene (Figure 3c).^[40] Only 1.0 wt% of Cu was

uniformly distributed on the surface of MXene, where Cu coordinated with three O with coordination bonds of 1.55 Å.

In addition to the O and F atoms introduced during the preparation of MXene, it is feasible to adding additional other heteroatoms for coordination atoms. The introduction of heteroatoms can not only increase the specific anchorage sites, but also further regulate the electronic structure of metal atoms, which is conducive to the improvement of catalytic activity. High-temperature annealing can also reduce the adsorbed metal ions. After annealing in argon at 550 °C for 120 min, Liu et al. doped Ru and N atoms into MXene at the same time, using RuCl₃ and melamine as precursors.^[41] S and P heteroatoms are also doped for the synthesis of single atoms. Therefore, the strategy is efficient to achieve high-performance SACs due to the provision of an easily regulated coordination environment.

3.2. Anchoring at the M Vacancies

3.2.1. Theoretical Basis

Defect engineering refers to that the TM atoms are fixed to the carrier through strong interactions with unsaturated–coordination vacancies. Metallic vacancies are natural sites on MXene that are highly reactive and can be used to anchor individual atoms. Li et al. calculated the forming energy of Zr, Hf, Ta,

W, Re, and Os filling on the bimetallic MXene $\text{Mo}_2\text{TiC}_2\text{O}_2$ with Mo defects, which were -1.89 , -2.24 , -1.64 , -0.10 , $+1.29$, and $+1.96$ eV, respectively. It is worth noting that the synthesized $\text{Mo}_2\text{TiC}_2\text{O}_2\text{-Pt}_{\text{SA}}$ showed more positive formation energy of $+2.62$ eV, indicating that the experimental preparation of $\text{Mo}_2\text{TiC}_2\text{O}_2\text{-Zr}_{\text{SA}}$ is feasible. Additionally, single atoms can be fixed to replace MXene lattice internal M atoms. Gao et al.^[1] found that Ru and Os filling on the Ti_3C_2 Ti showed the lowest forming energy. Therefore, metal M vacancy is a suitable monatomic fixation site, which is conducive to the formation of SACs.

3.2.2. Synthesis Method

In the synthesis process of MXene, the metal atoms on the surface will be unavoidably stripped to form metal vacancies, which have unsaturated coordination and certain reducibility. Through the self-reduction method, Zhao et al. fixed Pt onto the Ti vacancy of Ti-based MXene, and the loading amount of Pt was 0.2 wt %.^[42] Without additional reductant, the adsorption and reduction of Pt^{4+} occurred simultaneously (Figure 4a). The Pt atom was anchored at the Ti site rather than the lattice gap, which was proven by the clear Pt spots located at the lattice plane walls of the Ti columns (Figure 4b,c). The M vacancy of MXene is related to the concentration of etching agent and etching time. Park et al. etched V_2CT_x with 49% HF for 5 days, and the obtained V vacancies can be used to anchor-isolated Pt atoms by self-reduction.^[43] Also, Ni SACs/ $\text{Ti}_3\text{C}_2\text{T}_x$, with Ni content of 2.93 wt%, has been synthesized using the reactivity of Ti vacancies.^[44]

Assisted reduction method refers to the reduction of metal ions to single atoms by additional auxiliary processing after adsorption occurred. In CO_2 atmosphere, Zhao et al. calcined Se powder and Ti_3C_2 at 350°C for 120 min, and obtained 4.99 wt% Se SA injected into Ti-vacant $\text{Se-Ti}_3\text{C}_2$ (Figure 4d).^[45] Different from inert gases, CO_2 promoted the formation of Ti vacancy by reacting with Ti. In addition, the oxidation of CO_2 atmosphere was conducive to the generation of $-\text{O}$ terminal and the approach of Se to Ti vacancy, because the adsorption energy of Se on the O-MXene is far less than that on the F-MXene . Moreover, Se-C and Se-O bonds were observed, demonstrating the filling of Se atoms in the Ti vacancies. However, under the condition of argon, Se species synthesized by the same method was not fixed into Ti vacancy, but aggregated to form nanoparticles. For $\text{V}_\text{M}\text{-SACs}$ prepared by reduction method, the number and distribution of M vacancies will affect the loads of TM atoms and further affect the catalytic activity. Simply adding M vacancies increases the theoretical load of TM, but damages the structural stability of MXene.

The construction of quaternary hybrid MAX is a simple and fast method to obtain isolated metal sites, in which the single atom is completely embedded in the lattice. When the metal layer of A is removed with an etching agent, two different metals, including the target single-metal atoms, will be retained in the MXene. Kuznetsov et al. synthesized $\beta\text{-Mo}_2\text{C:Co}$ with the mixture of $(\text{NH}_4)_6\text{Mo}_7\text{O}_{24}\cdot 4\text{H}_2\text{O}$ and $\text{Co}(\text{NO}_3)_2\cdot 6\text{H}_2\text{O}$, and then successfully constructed a bimetallic MAX ($\text{Mo}_2\text{Ga}_2\text{C:Co}$) by adding metal Ga.^[46] Subsequently, $\text{Mo}_2\text{Ga}_2\text{C:Co}$ was treated with HF, etching the metal Ga and excess Co atoms away, and

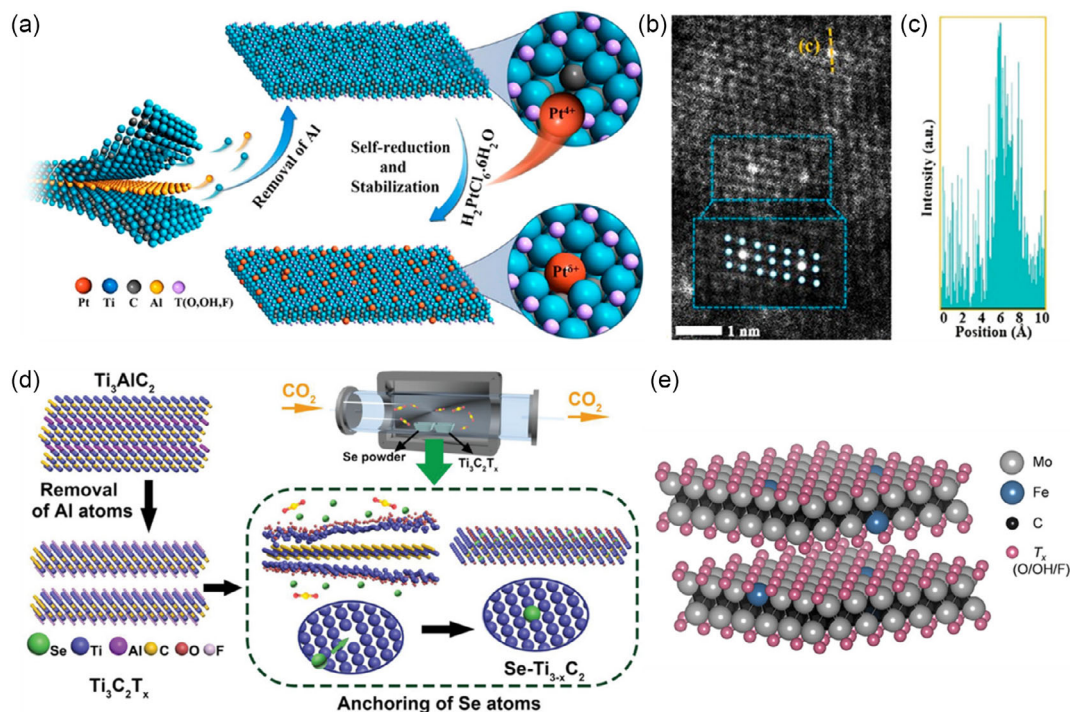


Figure 4. a) Self-reduction-stabilization process for the preparation of $\text{Pt}_1/\text{Ti}_{3-x}\text{C}_2\text{T}_y$. b) Magnified HAADF image of $\text{Pt}_1/\text{Ti}_{3-x}\text{C}_2\text{T}_y$. c) Corresponding intensity maps. Reproduced with permission.^[42] Copyright 2019, American Chemical Society. d) Synthesis process of the $\text{SASE-Ti}_3\text{C}_2$. Reproduced with permission.^[45] Copyright 2021, Wiley-VCH GmbH. e) Schematic representation of the $\text{Mo}_2\text{CT}_x\text{:Fe}$ structure. Reproduced under the terms of CC-BY license.^[47] Copyright 2021, The Authors, published by American Chemical Society.

$\text{Mo}_2\text{CT}_x\text{:Co}$ with 0.04 wt% Co single atom was finally obtained (Figure 4e). The MXene substrate synthesized by this method has a big transverse dimension of 1–2 μm . Further, this research group synthesized Fe SAs catalyst $\text{Mo}_2\text{CT}_x\text{:Fe}$ by the similar method, in which Fe content was 0.42 wt%.^[47] Both Fe and Co exhibited an oxidation state of +2, and the coordination environment are similar to that of Mo, suggesting that the construction of bimetallic MAX is a general strategy for the synthesis of single-atom sites anchored in M vacancies. Under high temperature and high pressure, quaternary hybrid MAX with different metal proportions can be synthesized, and MXene-based SACs with stable structure can be obtained more controllably.

3.3. Anchoring at the T Vacancies

3.3.1. Theoretical Basis

The functional groups –O, –F, and –Cl are easy to form defects or be replaced in the reaction process, which provides convenient conditions for the anchorage of metal single atoms in MXenes. Due to the high stability of O-terminated MXenes, more studies have focused on oxygen vacancies. The oxygen vacancy on the $\text{Mo}_3\text{C}_2\text{O}_2$ can be formed in reducing atmosphere (H_2 or CO).^[48] Cheng et al. studied the adsorption of Pd at different sites

on the surface of Mo_2CO_2 , and found that Pd anchored onto oxygen vacancies showed high stability and had good CO oxidation activity.^[25] With an energy barrier of 2 eV to diffuse to other nearby adsorption sites, Pd anchored on oxygen vacancies had a little tendency to migrate and form clusters. In the Mo_2CO_2 system constructed by Cheng et al., the formation energy of oxygen vacancy was 3.64 eV.^[49] Furthermore, the binding energy of Fe, Co, Ni, Cu, Zn, Ru, Rh, Ag, Ir, Pt, and Au atoms to the oxygen vacancies of Mo_2CO_2 was calculated. Four initial sites for anchoring TMs were calculated, including B, H_1 , H_2 , and oxygen vacancy (Figure 5a,b). However, no matter where the initial adsorption site was, TMs (except Fe) would always move to more stable oxygen vacancy during structural optimization. Moreover, the formation of metal nanoparticles in oxygen vacancies is more difficult than that of individual metals. Thus, it is practicable to synthesize the vacancies at T sites on MXenes by experiment and to use them for anchoring isolated metal atoms.

3.3.2. Synthesis Method

TM atoms can be directly anchored to T vacancies or substituted for the T atoms to form SACs. Unlike the surface adsorption behavior, metal anchoring at the T-vacancy implies doping into

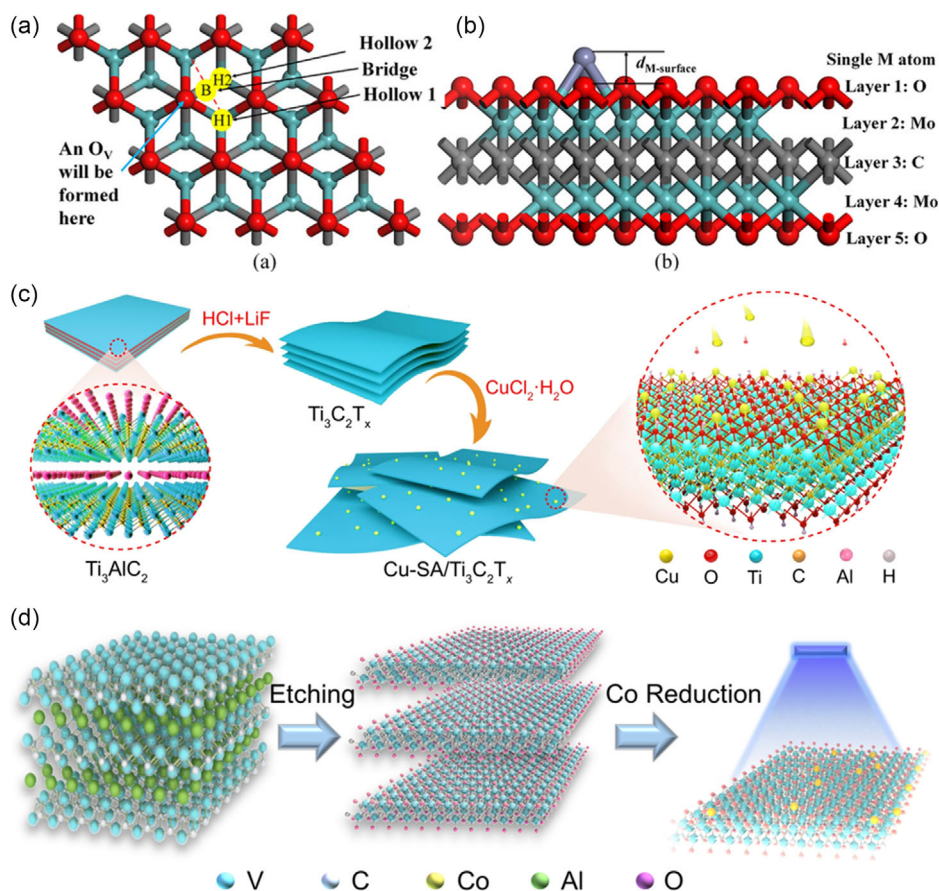


Figure 5. a) Top view of the pristine Mo_2CO_2 sheet. b) Side view of the optimized $\text{M}/\text{Mo}_2\text{CO}_2\text{-}_s$ structure. Reproduced with permission.^[49] Copyright 2019, Wiley-VCH GmbH. c) The synthesis of $\text{Cu-SA}/\text{Ti}_3\text{C}_2\text{T}_x$. Reproduced under the terms of CC-BY license.^[50] Copyright 2021, The Author(s), published by Springer Nature. d) The synthesis of $\text{Co}@V_2\text{CO}_2$. Reproduced under the terms of CC-BY license.^[51] Copyright 2022, The Authors, published by MDPI.

the MXene lattice. Bao et al. reduced $\text{Ti}_3\text{C}_2\text{T}_x$ with NaBH_4 , then added Cu ions, and finally obtained Cu SA/ $\text{Ti}_3\text{C}_2\text{T}_x$ by vacuum freeze-drying (Figure 5c).^[50] The distance between copper atoms was 0.61 nm, which was much larger than the length of Cu–Cu bond in the Cu dimer, indicating that there was no aggregation of Cu. Due to the coordination structure of Cu–O₃, the catalyst exhibits Faraday efficiency (FE) of 71% in the electrocatalytic reduction of CO to ethylene. Using freezing photochemical reduction method, Zhao et al. added CoCl_2 solution in the form of ice cube to V_2CT_x solution, and maintained the condition of 0 °C to ensure the slow release of Co^{2+} to avoid the formation of clusters (Figure 5d).^[51] The mixture was then exposed to ultraviolet light for 1 h to reduce and fix the Co onto the MXene. The Co–O and Co–V bonds were formed, demonstrating the successful doping of Co on V_2CT_x . The synthesis of Co SACs on Nb- and Ti-based MXene can also be achieved by this method.

The oxygen-functional groups of $\text{Ti}_3\text{C}_2\text{T}_x$ would be removed in the form of H_2O , leading to the form of oxygen vacancy during the process of high-temperature annealing. In Ar/ H_2 , Zhang et al. reduced Pt^{2+} to zero-valence Pt and anchored it on the generated oxygen vacancy at 400 °C.^[52] The oxidation state of Pt increased by bonding with Ti. Ramalingam et al. mixed sulfurea, Ru, and $\text{Ti}_3\text{C}_2\text{T}_x$ uniformly. After freeze-drying, it was annealed at 500 °C to obtain N-, S-, and Ru-co-doped $\text{Ti}_3\text{C}_2\text{T}_x$, where Ru was coordinated with N and S simultaneously.^[53] The photocatalytic hydrogen evolution reaction (HER) performance of $\text{Ru}_{\text{SA}}\text{-N-S-Ti}_3\text{C}_2\text{T}_x$ was higher than that reported on precious metal catalysts. Therefore, the performance of MXene-based SACs can be improved by the T-vacancy filling strategy. During the synthesis of SACs by this strategy, the construction of uniform T-vacancy anchoring sites needs to be optimized, and suitable metal precursors should be explicitly selected to form specific coordination structures to avoid the loss of defects.

4. Characterizations of Isolated Metal Atoms in MXenes

SACs have been widely used in various fields, but in the experimental process, the successful synthesis of single atoms needs accurate characterization to prove their dispersion.^[32] Existing methods for the characterization of single atoms fall into two main categories: 1) microscopic characterization, including scanning transmission electron microscope (STEM) and scanning tunneling microscope (STM) and 2) spectral characterization, including X-ray absorption spectroscopy (XAS), X-ray photoelectron spectroscopy (XPS), energy-dispersive X-ray spectroscopy (EDX), electron energy loss spectroscopy (EELS), and surface-enhanced Raman spectroscopy (SERS).

4.1. STEM

The rapid development of STEM makes the characterization of atomic-scale metals simple and intuitive. High-angle annular dark-field STEM (HAADF-STEM) clearly shows the existence of isolated single atoms, taking advantage of the difference of atomic number between metal atoms and the support. When electrons accelerated by high-voltage attack metal atoms with high atomic number, high-angle diffraction would be

produced, showing brighter images, while low-atomic number atoms cause small-angle electron scattering, showing dark-field images. The metals with higher atomic numbers produce brighter images. For MXene, 2D material-containing layers of TM atoms, the different kinds of metal atoms anchored to its surface can be identified by brighter or darker imaging. Zou et al. obtained a Ru-based SAC by equipping Ru atoms on the surface of $\text{Ti}_3\text{C}_2\text{T}_x$ by impregnation method (Figure 6a).^[54] The bright spots in the HAADF-STEM image corresponded to the highly dispersed Ru atoms and the enlarged HAADF-STEM image showed more pronounced Ru atoms anchored inside the lattice of $\text{Ti}_3\text{C}_2\text{T}_x$ (Figure 6b–d). The isolated Pt atoms on MXene aerogel were synthesized by Peng and coworkers (Figure 6e).^[55] The atomic dispersion of Pt was proven by highly dispersed bright spots in the HAADF-STEM. In addition, the distance between atoms was significantly larger than the radius of Pt, and Pt atoms were uniformly distributed in EDX spectra, which all demonstrated that no Pt nanoparticles were formed. More, other different types of single atoms on MXene have been detected via HAADF-STEM, such as Ir, Sb, Cu, Co, Cr, Ni, and Se.^[44,45,56–60]

The STM was invented in 1982 with a resolution of nanometers both horizontally and vertically, marking the dawn of a new era in which atoms could be observed directly. If a voltage is applied between the STM probe with less than 1 nm and the sample, there will be tunnel current due to tunnel effect. When the STM probe is scanned on the surface of the material, fluctuations of less than 0.1 nm will result in an exponentially varying tunnel current, achieving highly accurate detection of a single atom. However, the maximum resolution of STM can only be achieved on atomically flat samples. In addition, unlike STEM, STM can only detect the surface information of the sample.

4.2. XAS

The coordination environment of single atoms, including the electronic and geometric structure, can be studied through XAS spectra. In the characterization process, the electrons in the inner layer of a single atom are excited by high-energy electrons to the vacant orbitals in the outer layer that participate in bonding, while the excess energy that is not absorbed eventually causes oscillation of signal. Therefore, the absorption edge in the XAS spectrum has a characteristic, which is related to both the central atom and the coordination atom. Depending on the energy range, XAS can be divided into X-ray absorption near-edge structure (XANES) and extended X-ray absorption fine structure (EXAFS), which provide information on the oxidation states and coordination chemical bonds of the central atoms, respectively. For the XANES, it is more sensitive to chemical information such as valence states, unoccupied electron orbitals, and charge transfer. The higher the oxidation state of the atom is, the more the absorption moves toward the high-energy direction. XANES spectroscopy can also provide 3D structure information for the complement of EXAFS to a certain extent. EXAFS can provide the coordination number of single atoms, coordination atoms, the bond length, and the average ligand structure plane.

Yang et al. synthesized different amounts of Pt on TiN and studied the coordination environment of Pt.^[61] For 0.35 wt%

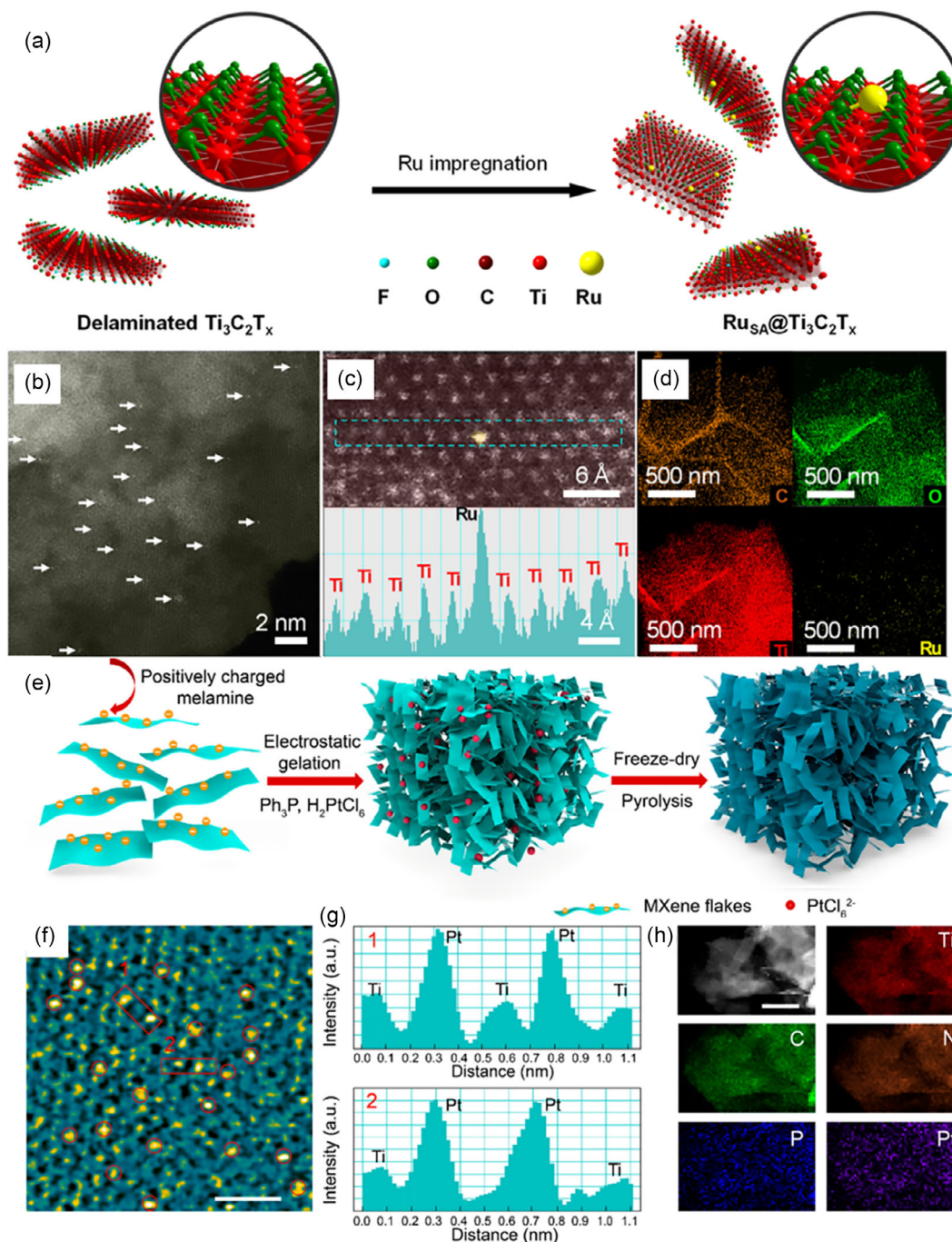


Figure 6. a) Fabrication procedure of RuSA@Ti₃C₂T_x. b) HAADF scanning transmission electron microscope (HAADF–STEM) image, c) Magnified HAADF–STEM image and the contrast profile of the highlighted region, and d) energy-dispersive X-ray spectroscopy (EDX) images of RuSA@Ti₃C₂T_x. Reproduced under the terms of CC-BY license.^[54] Copyright 2022, The Authors, published by MDPI. e) Synthetic route of Pt SA–PNPM. f) HAADF–STEM image of Pt SA–PNPM. g) The line-scanning intensity profile in the area marked by red rectangles in (e). h) STEM–EDX mapping of Pt SA–PNPM. Scale bars: f) 1 nm, h) 100 nm. Reproduced with permission.^[55] Copyright 2022, American Chemical Society.

Pt sample, the EXAFS spectra show that the strong peak at 2 Å corresponds to the presence of Pt–Cl, and its coordination number is 3.038, much larger than that of Pt–Pt (0.583). Zhao et al. synthesized Pt₁/Ti_{3–x}C₂T_y for CO functionalization.^[42] In the EXAFS spectra, the peak at 1.5 Å was attributed

to the first shell of Pt–C with coordination number of 3.1 ± 0.8 and bond length of 1.99 ± 0.02 Å, and the peak at 2.2 Å was attributed to the higher shell of Pt–Ti with coordination number of 3.8 ± 0.6 Å and bond length of 2.68 ± 0.02 Å. The incorporation of Pt atoms resulted in a slight increase in

the oxidation state of Ti, but did not change the structure of MXene. Zhou et al. used XANES analysis to uncover that the oxidation number of Pt in Pt SAs/ $\text{In}_2\text{S}_3/\text{Ti}_3\text{C}_2$ was between 0 and 4. In the Fourier transform (FT-) EXAFS spectrum, the peak of Pt-S is located at 2.2 Å and the coordination number is 2.71 (Figure 7a,b).^[62] Jin et al. characterized Fe single atoms on the surface of bimetallic MXene, and found that the absorption edge position was located between the absorption edge of bivalent and trivalent FeO_x .^[63] The peak at 1.42 Å is corresponded to the Fe-O bond, and the fitting results indicated that Fe-O₆ was the main structure (Figure 7c,d). Single Fe atoms synthesized by Kuznetsov et al. exhibited different oxidation states and

coordination environments.^[47] The edge absorption was close to that of FeO, indicating an oxidation state of +2. In addition, two characteristic peaks in the XANES spectrogram, located at 7121.5 and 7127.9 eV, respectively, were simulated to prove the substitution of Fe to Co (Figure 7e-g).

In addition to structural analysis of single-atom sites, in situ XAS technique has been widely used to study catalytic mechanisms. Nitrogen reduction reaction (NRR) catalytic behavior of Ru atom on Mo vacancy in Mo_2CT_x has been studied by Peng et al. through operando XAS measurements.^[64] The oxidation state of Ru in nitrogen was higher than that in argon, which was attributed to the electrons transfer from Ru to N_2 . In the

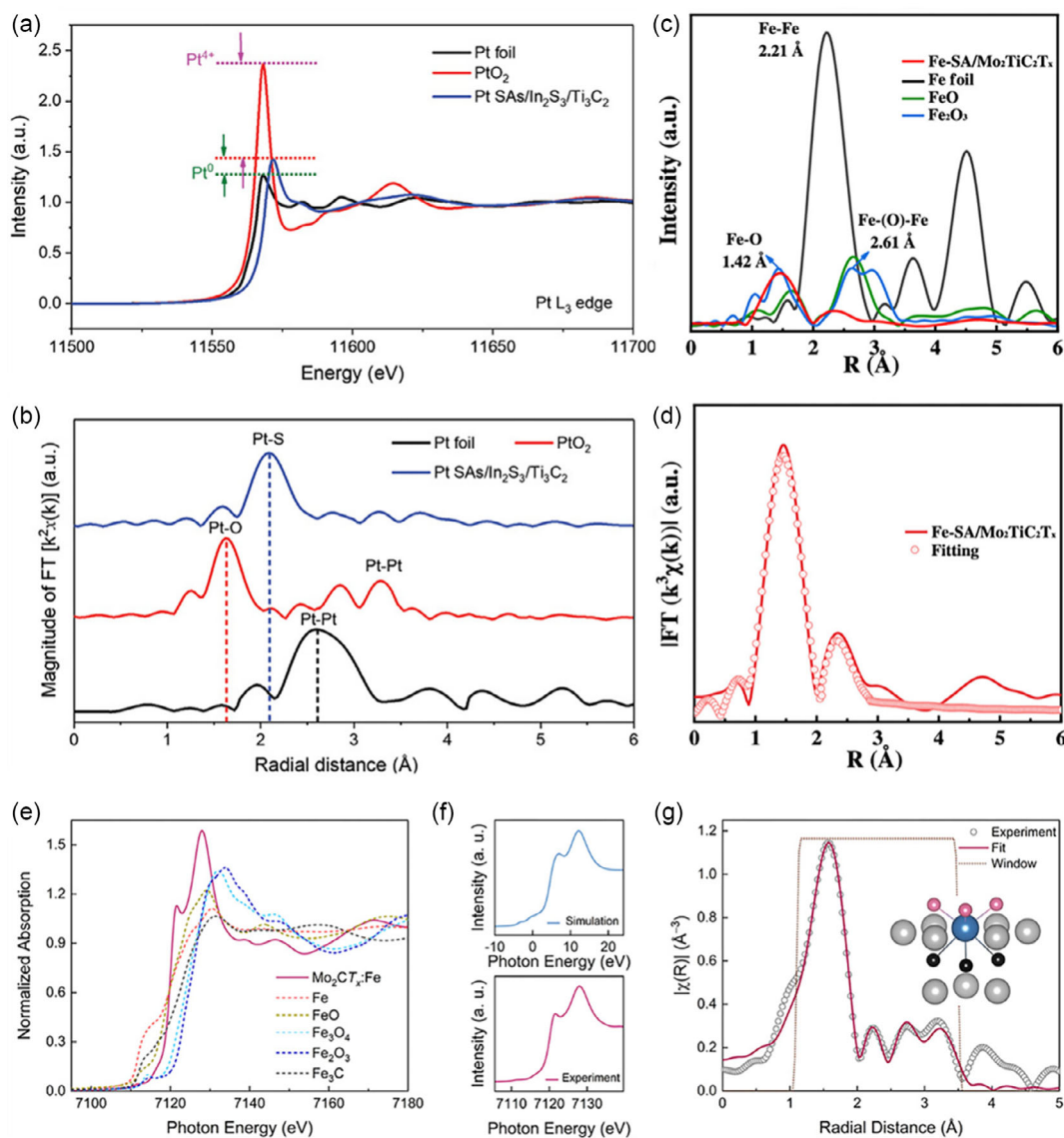


Figure 7. a) X-ray absorption near-edge structure (XANES) spectra of Pt foil, PtO_2 , and Pt SAs/ $\text{In}_2\text{S}_3/\text{Ti}_3\text{C}_2$ at the Pt L_{3} -edge. b) Fourier transform (FT) of the X-ray absorption fine structure (EXAFS) at the k^3 -weighted R space for Pt SAs/ $\text{In}_2\text{S}_3/\text{Ti}_3\text{C}_2$ and the Pt foil and PtO_2 as reference samples. Reproduced with permission.^[62] Copyright 2022, Wiley-VCH GmbH. c) FT-EXAFS spectra of Fe-SA/ $\text{Mo}_2\text{TiC}_2\text{T}_x$. d) FT-EXAFS fitting spectrum. Reproduced with permission.^[63] Copyright 2022, American Chemical Society. e) Normalized Fe K-edge XANES spectra of $\text{Mo}_2\text{CT}_x\text{-Fe}$ and reference materials. f) Comparison between the experimental XANES spectrum of $\text{Mo}_2\text{CT}_x\text{-Fe}$ and the theoretical simulation. g) Phase-uncorrected FT of the Fe K-edge EXAFS function for $\text{Mo}_2\text{CT}_x\text{-Fe}$. Reproduced under the terms of CC-BY license.^[47] Copyright 2021, The Authors, published by American Chemical Society.

FT-EXAFS spectrum, the main peak located at 1.58 Å was negatively shifted due to the formation of Ru-N. It is worth noting that the decrease of oxidation state of Ru and positive shift of main peak after voltage application indicated that Ru single atom could be reused for adsorption and desorption of N₂. Combined with theoretical calculations, the electron donating effect of Ru exhibited a positive effect on the activation of N₂ and the first hydrogenation. Djire et al. obtained enhanced HER activity by replacing Ti atoms in Ti₄N₃(OH)_x with Cr and Mo, and studied the change of metal valence state during HER process by in situ XANES analysis.^[65] For Mo-Ti₄N₃T_x, the EXAFS spectra showed peaks at 1.2 and 1.8 Å, corresponding to the first shell and Mo-O and the second shell of Mo-Ti, and the peak at 1.2 Å became smaller with the increase of applied voltage, indicating the decrease of Mo-O. Since the oxidation state of Mo did not change significantly, the reduction of Ti⁴⁺-Ti³⁺ and the induction of oxygen vacancy were inferred to be the main source of HER activity. For Cr-Ti₄N₃T_x, however, a different HER mechanism was put forward. During HER simulation, the reduction of Cr³⁺ to Cr²⁺ was observed and was thought to promote the formation of O vacancy and subsequently improve HER activity.

4.3. XPS

The highly dispersed metal atoms usually exist in an unsaturated state and have electron states different from metals oxides, which can be analyzed by XPS spectra. Under X-ray irradiation, electrons with certain kinetic energy are excited from the surface atoms in SACs, and the resulting spectra are used for qualitative and quantitative analysis of the surface atoms.^[66,67] For specific monochromatic excitation sources and specific atomic orbitals, the photoelectron energy is characteristic. When the excitation source energy is fixed, the photoelectron energy is only related to the type of element and the atomic orbital excited by ionization. In addition, the chemical environment of atoms is different as the shift of the spectral peak. Yi et al. reduced H₂PtCl₆ to Pt and fixed it on the heterojunction constructed by N, B, and F-doped ReS₂ (NBF-ReS₂) and Mo₂CT_x.^[68] The binding energy of the fixed Pt was close to that of the zero-valent Pt, with a positive chemical shift of 0.9 eV, which proved that the Pt single atoms are successfully synthesized and strongly interacted with the carrier (**Figure 8a**). SA Pt catalysts synthesized by Cui et al., with different amounts of Pt, all exhibited zero-valent oxidation state and forward chemical shift (**Figure 8b**).^[69] Nonmetallic B

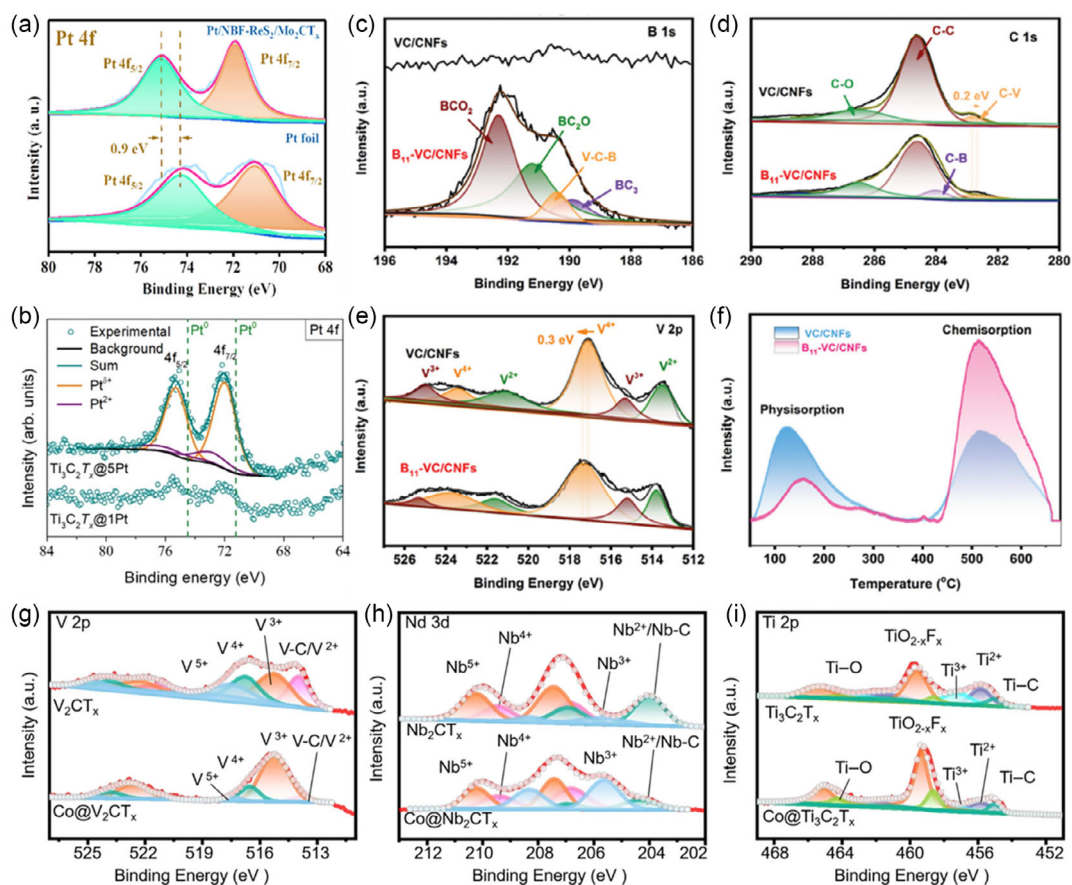


Figure 8. a) Pt 4f X-ray photoelectron spectroscopy (XPS) spectra of Pt/NBF-ReS₂/Mo₂CT_x and Pt foil. Reproduced with permission.^[68] Copyright 2021, Elsevier. b) Pt 4f peaks of Ti₃C₂T_x@1Pt and Ti₃C₂T_x@5Pt. Reproduced with permission.^[69] Copyright 2020, Wiley-VCH GmbH. c) B 1s, d) C 1s, and e) V 2p XPS spectra of VC/CNFs and B₁₁-VC/CNFs. f) N₂ temperature programmed desorption curves of VC/CNFs and B₁₁-VC/CNFs. Reproduced with permission.^[70] Copyright 2021, Wiley-VCH GmbH. XPS spectra of g) V 2p in Co@V₂CT_x and V₂CT_x; h) Nb 3d in Co@Nb₂CT_x and Nb₂CT_x; i) Ti 2p in Co@Ti₃C₂T_x and Ti₃C₂T_x. Reproduced under the terms of CC-BY license.^[51] Copyright 2022, The Authors, published by MDPI.

atoms formed B–C–V bonds on the surface of vanadium carbide, in which electrons flowed from B and V to C.^[70] The B doping caused V 2*p* binding energy to move forward, and the content of V in the high state increased, suggesting the electron contribution of V to C (Figure 8c–e). In addition, the B–C–V enhanced the adsorption of nitrogen on the catalyst, which was conducive to the nitrogen reduction reaction (Figure 8f). Zhao et al. anchored Co single atoms on the surface of V-, Nb-, and Ti-based MXenes.^[51] In the doping process, the oxidation of V, Nb, and Ti occurred to different degrees, which was attributed to the redistribution of charge (Figure 8g–i).

5. Applications of MXene-Based SACs

5.1. Applications in Electrocatalysis

5.1.1. Hydrogen Evolution Reaction

As a clean energy, hydrogen produced by electrocatalytic water splitting can be used as an alternative to fossil fuels. As the key substance in the process of electrolytic hydrogen production, the electrocatalyst of HER plays an important role in the industrialization of electrolytic water. High dispersion of precious metals (Pt, Ir, Ru, Rh, etc.) can improve the atomic utilization while maintaining high HER activity. By electrochemical stripping method, Zhang et al. fixed single-atom Pt on the Mo vacancy on the surface of bimetallic MXene to form stable Pt–C bond.^[71] Under acidic conditions, it achieved a current density of 100 mA cm^{−2} at an overpotential (η_{100}) of 77 mV, with a high mass activity (about 40 times than that of Pt/C), and could maintain stability for 100 h. Through a spontaneous reduction method, Cui et al. synthesized MXene@Pt, which kept stable for 800 h at the current density of 10 mA cm^{−2}.^[69] Using the reducibility of V₂CT_x, Park et al. fixed successfully 0.88 wt% Pt atoms in the V vacancy of V₂CT_x, exhibiting high HER activity in both acidic and alkaline media.^[43] Through the bonding of Pt with N and O, Kang et al. fixed Pt in nitrogen-doped Ti₃C₂, and the obtained catalyst showed high FE in a practical device.^[72] By electrostatic adsorption and high-temperature treatment, Peng et al. synthesized Pt sites on porous N- and P-co-doped MXene (PNPM) to obtain 3D Pt SA–PNPM, where N/P-coordinated Pt increased the intrinsic activity of the electrocatalyst.^[55] In addition, the Pt SA–PNPM catalyst displayed low overpotential and small Tafel slope comparable to Pt/C over a wide pH range, but had higher mass activity than Pt/C (Figure 9a–h). Zhang et al. replaced part of the surface oxygen atoms on MXene sheets with Pt by a rapid thermal shock technique. Theoretical calculations showed that Pt on oxygen vacancy reduced the adsorption of intermediate H, and the Gibbs-free energy was 0.02 eV (Figure 9i–o).^[52]

Ru SAs–MXene synthesized by Zou et al. showed excellent alkaline HER properties, which could reach the current density of 1 A cm^{−2} at the overpotential of 435 mV, in which the loading capacity of Ru was only 0.44 wt%.^[54] In addition, the mass activity of the Ru SAs–MXene increased with increasing potential and was two orders of magnitude higher than that of Pt/C at high current density. In addition, theoretical calculations showed that the adsorption of the intermediate H occurred on the three oxygen atoms adjacent to Ru atom rather than Ru atoms, where the

ΔG was close to 0 eV. Nitrogen- and sulfur-co-doped Ir^[58] or Ru^[53] in the surface of MXene also exhibited enhanced HER activity, which was attributed to the redistribution of the charge of the active metal atom, improving the adsorption of the intermediate H.^[39] By calculating the formation energy of the anchored TM at the Ti vacancy, Kong et al. found that TM tended to embed MXene as a single atom rather than a bulk metal, with a negative adsorption energy (Figure 10a,b).^[73] In addition, Mo–Ti₂N was a potential high-performance HER catalyst with a hydrogen adsorption-free energy close to that of Pt (Figure 10c). Kuznetsov et al. replaced part of Mo in Mo₂C with Co to form an isolated Co-based catalyst Mo₂CT_x:Co, similar to bimetallic MXene solid solution, where Mo and Co had the same coordination structure.^[46] Under acidic conditions, the HER activity of Mo₂CT_x:Co was significantly higher than that of Mo₂CT_x with the same load, and even better than that of Mo₂CT_x with ten times loading (Figure 10d–f). The increased activity was attributed to the perturbation of the electronic structure on the surface of MXene by Co doping, which made the adsorption of H by oxygen atoms more moderate and conducive to the occurrence of HER (Figure 10g–i). The doping of Ni at the Mo vacancy also exhibited low overpotential and fast kinetics.^[74] It is worth noting that most TM doping improves HER activity by promoting the reduction of Ti⁴⁺ to Ti³⁺ and inducing oxygen vacancy, while Cr doping is more inclined to the SAC-driven mechanism, in which the reduction of Cr³⁺ to Cr²⁺ occurs during HER process.^[65]

5.1.2. Oxygen Electrode Reaction

Bifunctional oxygen electrode is an important part of rechargeable metal–air batteries and reversible fuel cells.^[75,76] However, due to large overpotentials required to overcome the large reaction barriers of oxygen evolution reaction (OER) and oxygen reduction reaction (ORR), the energy efficiency of metal–air batteries and fuel cells is greatly reduced, which limits their industrialization. In recent years, MXene-based SA electrocatalysts have been widely studied for OER and ORR. Xu et al. loaded Pt nanoparticles onto MXene for the ORR, and meanwhile added CNT to suppress the distortion of Pt nanoparticles.^[77] The reduction of the atomic scale and the MXene substrate increased the mass activity of the catalyst by 3.4 times compared with Pt/C, even if the catalyst did not reach the single-atomic scale. Moreover, SA Pt was synthesized via a static method, and only 0.35% Pt was loaded on TiN carrier.^[61] The coordination number of Pt–Pt of 0.35 wt% Pt/TiN was 0.583, which was much smaller than that (8.310) of 5 wt% Pt/TiN, proving that there was no nanoparticles. During the ORR process, 0.35 wt% Pt/TiN mainly underwent two electron transformations, presenting high selectivity (65%) for H₂O₂. Liu et al. calculated the effect of surface-functional groups on single-Pt atoms, and the results showed that the –F was more conducive to the ORR catalysis than –O.^[27] If a certain degree of strain is applied, the metal d-band center and work function of MXene would shift, improving the electrocatalytic performance. The overpotential of Pt–V_F–Ti₂CF₂, with Pt loaded on the F vacancy, decreased significantly under 14% compressive strain and 4% tensile strain (0.28 V for ORR and 0.03 V for OER).^[78] Furthermore, Ma et al. studied the effect of supports on bifunctional ORR/OER performance and

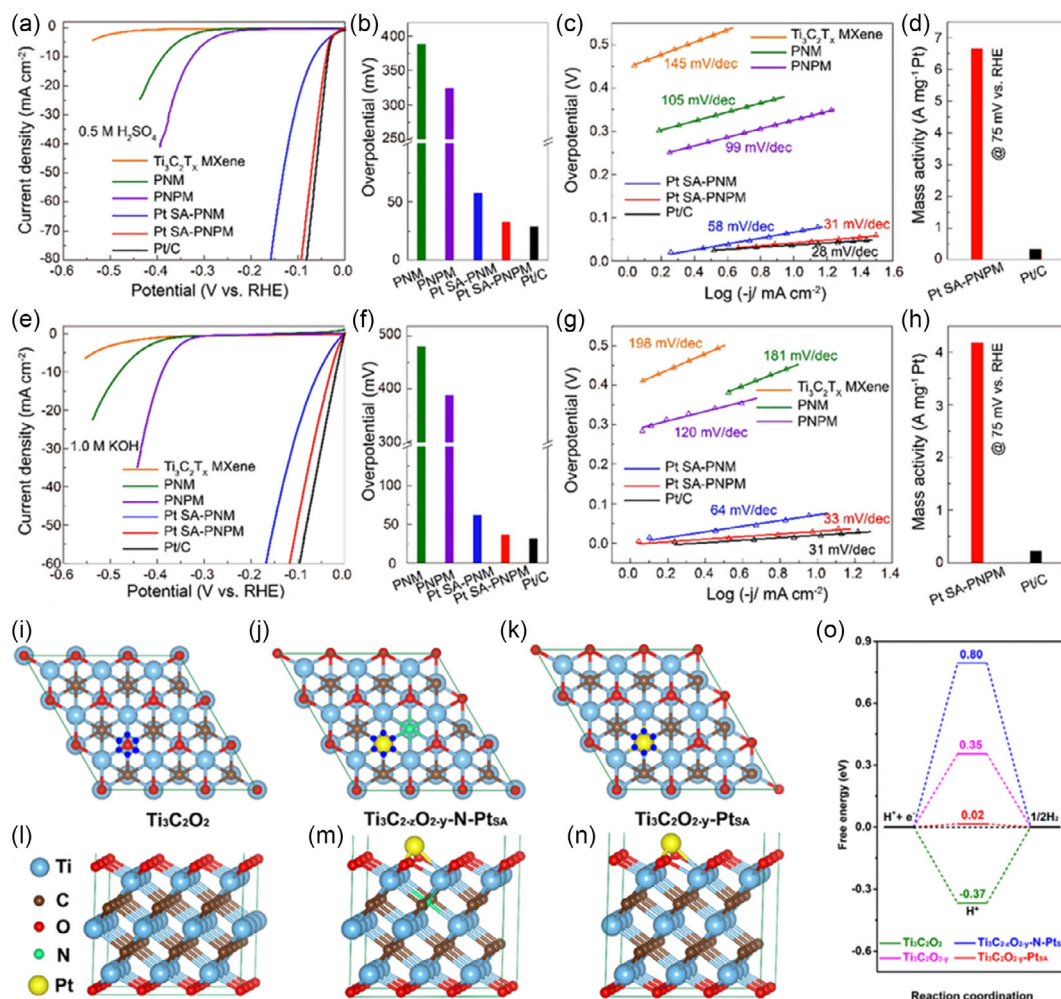


Figure 9. a–d) Electrochemical hydrogen evolution reaction (HER) performance of Ti₃C₂T_x MXene, porous N codoped MXene (PNM), PNPM, Pt SA-PNM, Pt SA-PNPM, and commercial Pt/C in 0.5 M H₂SO₄ and e–h) 1 M KOH. Reproduced with permission.^[55] Copyright 2022, American Chemical Society. Density functional theory (DFT) calculations of Ti₃C₂O₂-based catalysts for the HER. i–n) Atomic structures for Ti₃C₂O₂, Ti₃C_{2-x}O_{2-y}-N-Pt_{sa}, and Ti₃C₂O_{2-y}-Pt_{sa}, respectively. o) Calculated Gibbs-free energies of adsorbed hydrogen. Reproduced with permission.^[52] Copyright 2022, American Chemical Society.

discovered the η , η_{10} , and ΔE ($E_{\eta_{10}} - E_{1/2}$) of Pt-V₅-Ti₂CSBr, Pt-V₁-Ti₂COI, and Pt-V₅-Ti₂CSBr as ORR, OER, and ORR/OER catalysts were 0.35, 0.34, and 0.79 V, respectively.^[79]

Kuznetsov et al. synthesized a highly dispersed single-iron-atom catalyst by injecting 1 mol% iron atoms into the Mo vacancy of Mo₂CT_x.^[47] Under oxygen reduction conditions, Mo₂CT_x-Fe would degrade in situ to a carbon skeleton to form Fh/C, in which the ferric hydroxide species were the true active species to activate ORR (Figure 11a). Under alkaline conditions, the catalyst showed excellent ORR performance and its selectivity to H₂O₂ was still up to 90% when the applied voltage was greater than 0.4 V (Figure 11b–d). To adjust the electronic structure of Fe atoms, Liu et al. constructed an axial Fe–O–Ti structure with Ti₃C₂T_x as a substrate, which could change the spin state of Fe–N₃O site and improve its adsorption of O₂ (Figure 11e).^[80] In 0.1 M KOH, the catalyst had a half-wave potential ($E_{1/2}$) of 0.861 V and a mass activity of 182.1 mA mg⁻¹, which was 4.3 times better than that of the catalyst before optimization.

What's more, the catalyst that underwent the four-electron-transfer reaction provided greater power in the fuel cell.

The OER activity of SACs has been screened by theoretical calculations. Chen et al. studied the loading of a series of mid-to-late TM atoms on M₂NO₂ (M = Ti, V, Cr) and proved that Cu–Ti₂NO₂ was a hopeful electrocatalyst for the OER, with a low aggregation trend and a low theoretical overpotential of 0.24 V.^[81] Via a controlled pyrolysis to remove Zn atoms, Kou et al. successfully synthesized Cu-, Co-, and Ni-doped Mo₂C with imidazole salts as raw materials, in which Co-based Mo₂C showed the best OER/HER-bifunctional activity.^[82] For OER, the Co-based Mo₂C had a low η_{10} of 270 mV and high turnover frequency (1.37 times higher than that of Co SA without MXene), owing to the improved adsorption of OH* intermediate on the Co sites. Theoretical calculations revealed that the coordination structure of Co and three Mo broke the proportional relationship between adsorption energies of adjacent intermediates, increasing the intrinsic activity of the catalyst.

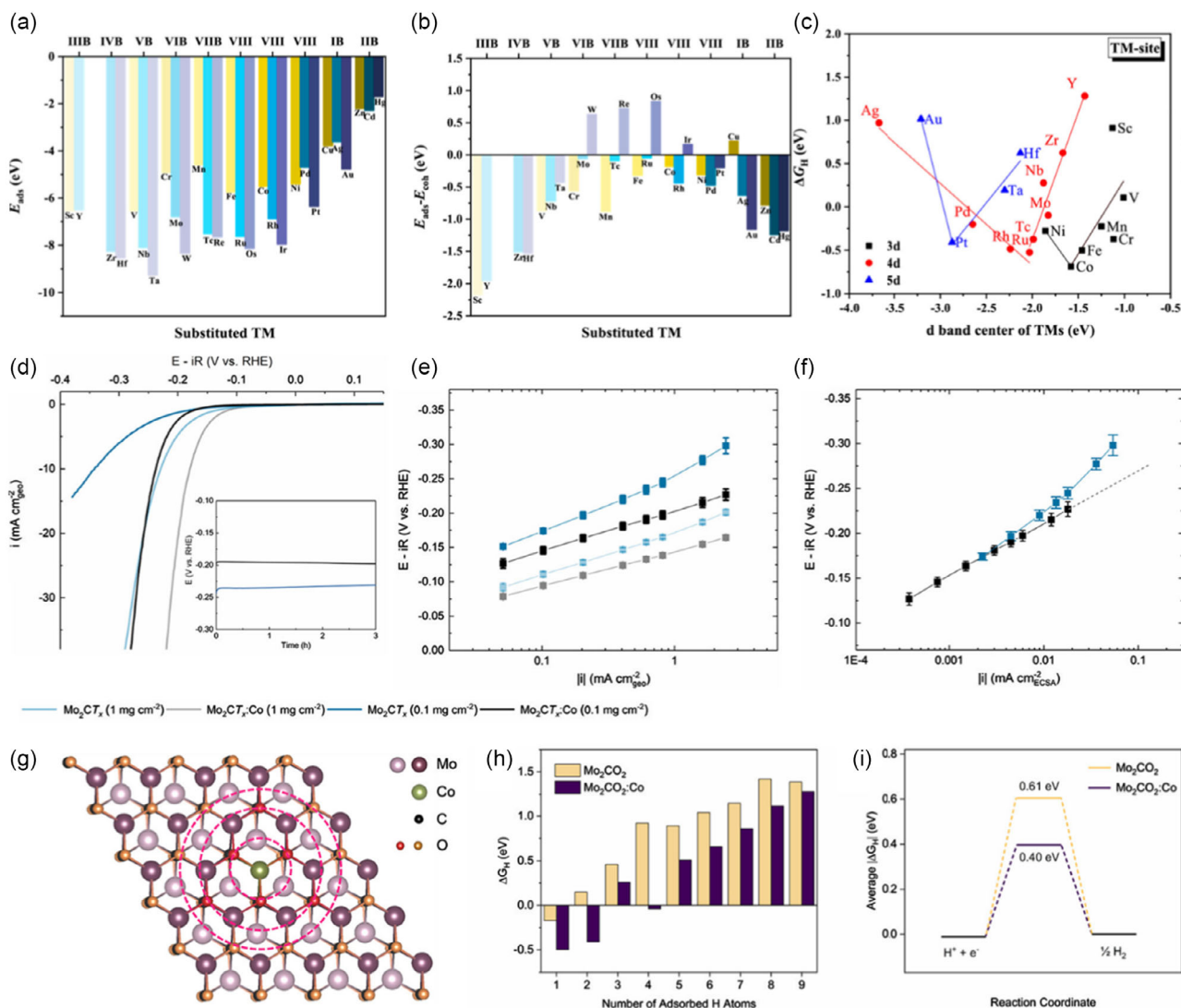


Figure 10. a) Adsorption energy (E_{ads}) and b) differences between adsorption energy and cohesive energy ($E_{\text{ads}} - E_{\text{coh}}$) of TM atoms. c) Correction of ΔG_H and d-band center value on TM sites. Reproduced with permission.^[73] Copyright 2022, American Chemical Society. d) Mo₂CO₂:Co model structure used for DFT calculations. e) Computed values of ΔG_H on Mo₂CO₂ and Mo₂CO₂:Co surfaces. f) Reaction coordinate for the hydrogen evolution on Mo₂CO₂ and Mo₂CO₂:Co. g) Mo₂CO₂:Co model structure used for DFT calculations. h) Computed values of the free energies of hydrogen adsorption (ΔG_H) on Mo₂CO₂ and Mo₂CO₂:Co surfaces. i) Reaction coordinate for the hydrogen evolution on Mo₂CO₂ and Mo₂CO₂:Co with average $|\Delta G_H|$ values computed for the hydrogen adsorption on six oxygen atoms shown in red on panel (g). Reproduced with permission.^[46] Copyright 2019, American Chemical Society.

Bifunctional oxygen electrodes with high OER and ORR activity are more practical applications in fuel cells and metal–air batteries. Kan et al. constructed Pt and Pd on MXene, and studied the influence of M (Nb, Ti, V, or Cr), X (C or N), and T (O or F) on the performance of SA electrocatalysts.^[83,84] Theoretical calculations indicated that the combination of Nb-based carbides, F-functional groups, and Pt doping displayed the best OER/ORR-bifunctional catalytic performance. Furthermore, Wei et al. constructed a dual-atom catalyst (DAC) model of double transition metal-doped MXene, and screened out Ni1/Ni2- and Fe1/Ni2-MXene with OER/ORR-bifunctional catalytic activities, which were even better than the Pt and IrO₂ (Figure 12).^[85] The electron induction between Fe, Ni, and oxygen atoms and moderate tensile strain changed the electronic structure of MXene

surface, which provided the theoretical basis for the design of bimetallic atom electrocatalysts for OER/ORR.

5.1.3. Carbon Dioxide Reduction Reaction

The electrocatalytic reduction of CO₂ to hydrocarbons is a green and economy strategy to mitigate the greenhouse effect.^[86] Copper-based catalysts are potential electrocatalysts for CO₂ reduction due to their ability to break C–O bonds and low HER competitiveness. By etching Al atoms from quaternary Ti₃(Al_{1-x}Cu_x)C₂, Zhao et al. synthesized SA–Cu–MXene with atomic copper immobilized on the surface of Ti₃C₂, where Cu was connected with end oxygen.^[40] In 0.1 M KHCO₃ saturated

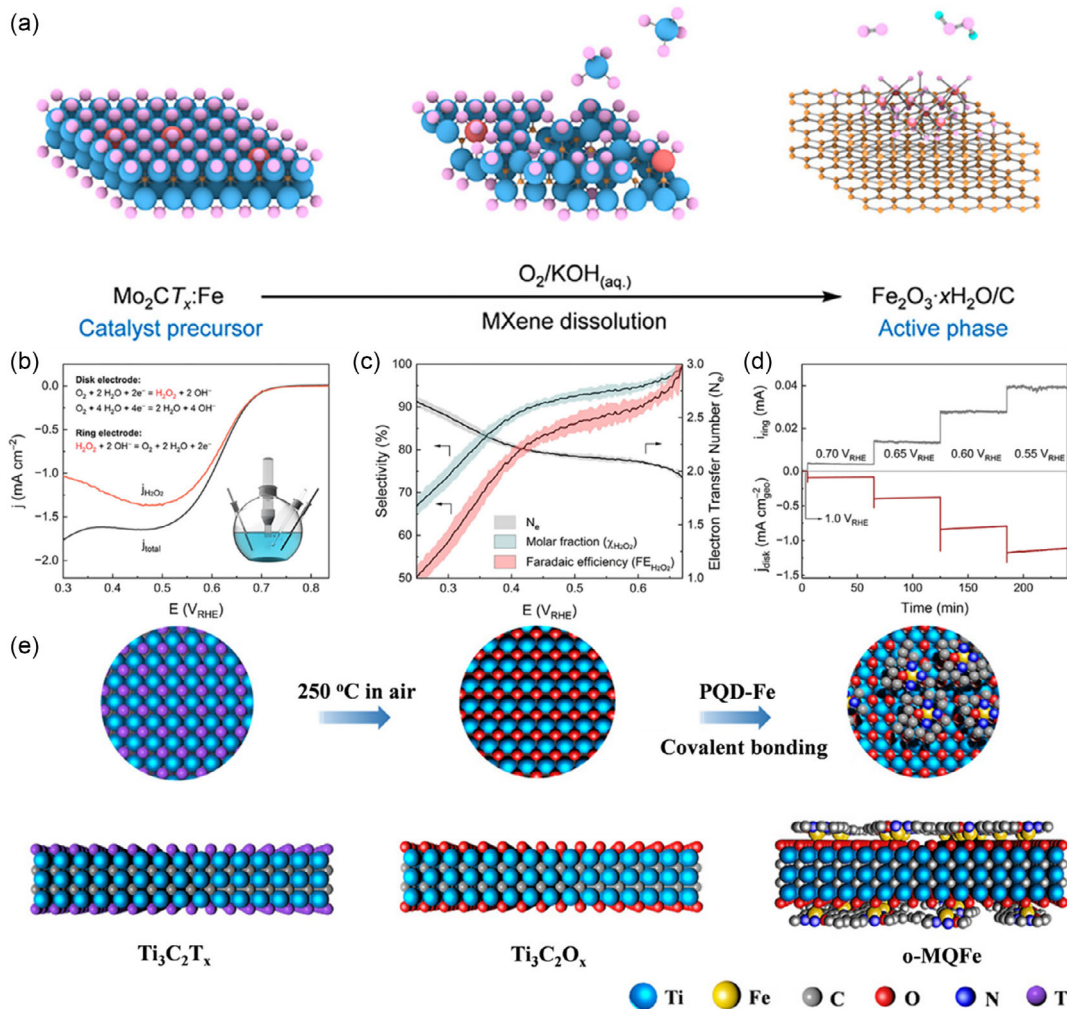


Figure 11. a) The degradation process of $\text{Mo}_2\text{CT}_x\text{:Fe}$. b–d) Electrocatalytic properties of Fh/C in O_2 -saturated 0.1 M KOH . Reproduced under the terms of CC-BY license.^[47] Copyright 2021, The Authors, published by American Chemical Society. e) The synthesis process of o-MQFe. Reproduced with permission.^[80] Copyright 2022, Wiley-VCH GmbH.

with CO_2 , SA-Cu-MXene reduced CO_2 to methanol, and when the applied voltage was 1.4 V, the FE of methanol production reached a maximum of 59.1%, much higher than that of Cu nanoparticles (Figure 13a–d). Theoretical calculations showed that the transformation from HCOOH^* to CHO^* was rate-determining step for the SA-Cu-MXene (Figure 13e,f). Furthermore, by simple standing method, 1.04 wt% of Cu was fixed to $\text{Ti}_3\text{C}_2\text{T}_x$, which reduced CO_2 to formic acid with an FE of 58.1%, four times that of $\text{Ti}_3\text{C}_2\text{T}_x$.^[87] Theoretical calculations showed that, in addition to Cu species, other transition metals, even Ti_2CO_2 also had a positive effect on the enhancement of CO_2RR activity.^[88] Oxygen-functional groups bonded with TM provided additional electrons into the $2\pi^*_u$ orbital of CO_2 , and split $2\pi^*_u$ into the $2\pi^*_u$ (unocc) orbital and $d-2\pi^*_u$ (occ) orbital (Figure 13g). Such orbital rebuilding resulted in the transformation of CO_2 structure from linear to V-shaped, which is conducive to the first hydrogenation step. In addition, the maximum Gibbs-free energy (ΔG_{max}) on Cr-anchored Ti_2CO_2 during CO_2RR was smaller than that during HER,

presenting high CO_2RR selectivity. In addition, Co- $\text{Ti}_3\text{C}_2\text{T}_x$ was also synthesized for the CO_2RR through a coordination process facilitated by electrostatic interaction (Figure 13h).^[36]

In addition, nonmetallic SA doping significantly improves the CO_2RR performance of MXenes. By calcining in ammonia, Qu et al. introduced nitrogen atoms and Ti vacancies into MXene, which effectively reduced CO_2 to CO in seawater.^[89] The maximum values of FE_{CO} (92%) and j_{CO} (-16.2 mA cm^{-2}) could be reached at -0.7 and -0.8 V, respectively, which were equivalent to the best electrocatalysts including precious metals. The coordination of nitrogen atoms and Ti vacancies improved the electronic structure of active sites and regulated the adsorption and desorption of intermediates.

5.1.4. Nitrogen Reduction Reaction

The industrial production of ammonia mainly relies on Haber-Bosch method, which needs high temperature and high pressure. Electrocatalytic NRR is a promising green alternative to

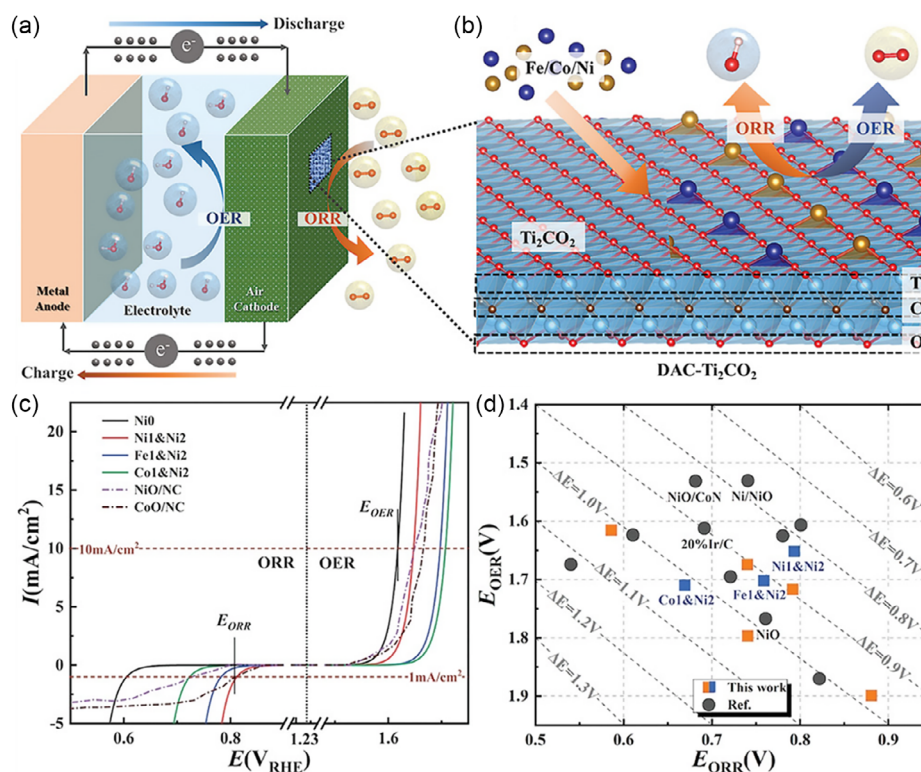


Figure 12. a) Configuration of a rechargeable metal–air battery. b) Electrocatalytic mechanisms for the formation of Fe/Co/Ni–DACs based on Ti_2CO_2 and for the oxygen evolution reaction/oxygen reduction reaction (OER/ORR). c) Theoretical polarization curves for NiO–SAC, Ni1&Ni2–DAC, and Fe1&Ni2–DAC and experimental curves for reported bifunctional electrocatalysts in the full range of ORR/OER potentials. d) Calculated ORR and OER activities of bifunctional catalysts. Reproduced with permission.^[85] Copyright 2021, Wiley-VCH GmbH.

fix N_2 at room temperature and pressure. Boron catalyst has been widely applied in the field of NRR, and adding nonmetal boron into the MXene can effectively promote the reduction of N_2 . Wen et al. synthesized vanadium carbide containing a high concentration of B atoms, in which the redistribution of electrons on the B–C–V bond regulated the adsorption of N_2 and reduced the reaction energy barrier.^[70] The ammonia yield of the catalyst was $0.443 \text{ mol h}^{-1} \text{ cm}^{-2}$ and the FE was 46.1% in 0.5 M K_2SO_4 solution (Figure 14a,b). The electron-deficient property of B makes it have a high tendency to combine with electron-rich N, which is conducive to the first hydrogenation, but not favorable to the last hydrogenation. However, transition metals in MXene can adjust its electron-donating capacity to medium, which is advantageous to the release of NH_3 (Figure 14c–f).^[90] For NRR, the theoretical limit potentials of B– Mo_2CO_2 and W_2CO_2 were only -0.2 and -0.24 V, respectively. In addition, B@ $\text{V}_3\text{C}_2\text{O}_{2-x}$ was also predicted to display ideal NRR catalytic performance.^[91] Additionally, single-carbon atoms injected into the oxygen vacancy of MXene showed NRR activity.^[92] As interacting with adjacent TM atoms, the electron filling in the P_z orbitals of active carbon atoms changed, further promoting the activation of N_2 . With low limit potential (-0.14 – -0.38 V), single-C atoms on Nb_2CO_2 , Mo_2CO_2 , and W_2CO_2 were screened as active NRR catalysts with high selectivity.

Peng et al. fixed single-ruthenium atoms into the Mo site of Mo_2CT_x for NRR under mild conditions, where Ru content was

1.41 wt% (Figure 15a).^[64] At -0.3 V, Ru– Mo_2CT_x had an ammonia yield of $40.57 \mu\text{g h}^{-1} \text{ mg}^{-1}$, more than double that of commercial Ru/C, and an FE of 25.77%. Theoretical calculations indicated that the interaction between Ru $3d$ and C $2p$ orbitals was stronger than the hybridization between Mo $3d$ and C $2p$, making the adsorption and activation of N_2 easier, while making the reaction barrier of the speed control step lower. Since Ru– O_4 has the lowest formation energy on the surface of MXene compared with the combination of Ru with other functional groups, Ru SAs/ $\text{Ti}_3\text{C}_2\text{O}$ catalyst was synthesized by Chen et al via an alkali treatment method.^[37] At a low voltage of -0.2 V, the catalyst achieved high ammonia yield ($27.56 \mu\text{g h}^{-1} \text{ mg}^{-1}$) and FE (23.3%), which could remain stable for 20 h (Figure 15b–g). The Ru– O_4 site as the active center of NRR catalyzed the reaction by a more favorable distal/alternating hybrid path, with a significantly reduced ΔG_{max} of 0.78 eV, where the hydrogenation from $^*\text{NNH}_2$ to $^*\text{NHNH}_2$ was the rate-limiting step.

In general, the adsorption strength of the intermediate on the catalyst can serve as a descriptor of the NRR theoretical overpotential, and the first protonation of N_2 and the last generation of NH_3 determine the overall NRR overpotential.^[93] Gao et al. calculated the theoretical overpotential of N_2 activation and reduction when TM was anchored to $\text{Ti}_3\text{C}_2\text{O}_2$, and found that the load of single-Fe, Co, Ru, or Rh atoms had NRR activity.^[94] Furthermore, the NRR overpotential as low as 0.16 V was calculated on $\text{Mo}@\text{Mo}_2\text{CO}_2$, which catalyzed NRR through distal or

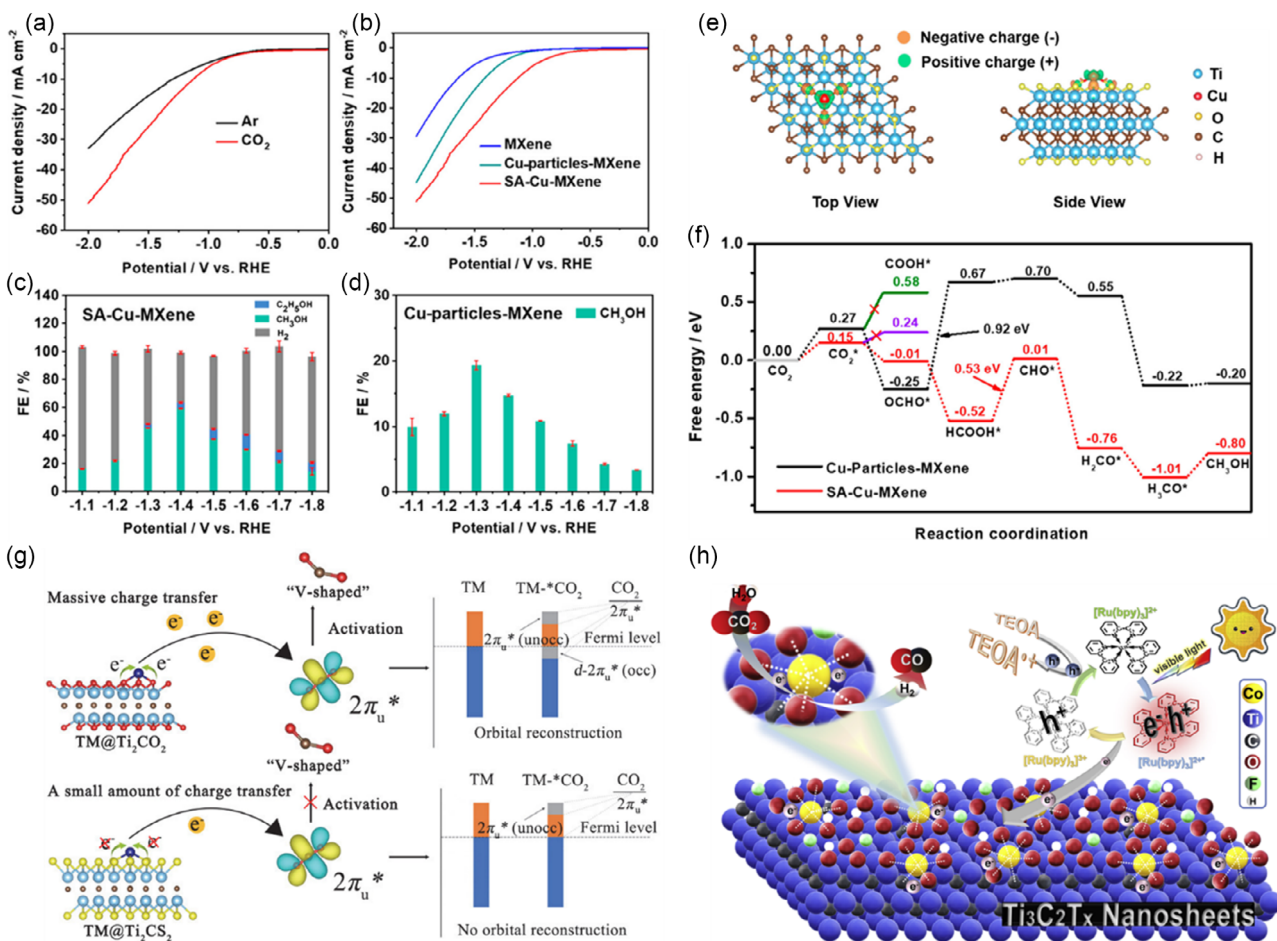


Figure 13. a,b) Linear sweep voltammetry (LSV) curves of SA-Cu-MXene in 0.1 M KHCO₃. Faraday efficiencies (FEs) of c) SA-Cu-MXene and d) Cu-particles-MXene. e) Charge density difference of SA-Cu-MXene. f) Free energy diagram of CO₂ to CH₃OH on Cu-O₃ structure. Reproduced with permission.^[40] Copyright 2021, American Chemical Society. g) Schematic diagram of CO₂ activation mechanism on TM/Ti₂CT_x. Reproduced with permission.^[88] Copyright 2022, Dalian Institute of Chemical Physics, Chinese Academy of Sciences. h) Mechanism of photocatalytic CO₂ reduction. Reproduced under the terms of CC-BY license.^[36] Copyright 2021, The Author(s), published by Elsevier.

hybrid mechanism.^[95] The covering of other nonmetallic functional groups (-OH, -F or -S) on MXene could further reduce the limiting potential compared to the covering of pure oxygen-functional groups.^[96] For example, the presence of -OH accelerated the adsorption of N₂ and the desorption of NH₃.^[97] On the surface of nitride Ti₂N₂O₂, single-Mo atom exhibited the best NRR performance ($\Delta G_{\text{NH}_3} = 0.12$ eV), with high inhibition for HER and high conductivity, accelerating electron transfer.^[98] In addition, other 2D MXenes have been screened as suitable carriers of single-TM-atom catalysts for electrocatalytic NRR.^[99–103]

5.2. Applications in Energy Storage

MXene modification can make it show better performance in the battery system.^[104] Ion reserve and capacity retention are the indicators to evaluate the performance of ion battery.^[105] The insertion of Co²⁺ ions into V₂C doubled the Li-ion capacity of the electrode material from 686.7–1117.3 mA h g⁻¹ at 0.1 A g⁻¹, owing to the interlayer expansion induced by V-O-Co (Figure 16a–c).^[56] Further, the V-O-Sn structure was

synthesized in the Sn/V₂C electrode by ion exchange, achieving a high lithium capacity (1284.6 mA h g⁻¹ at 0.1 A g⁻¹) and maintaining stability for 1600 cycles (Figure 16d–f).^[106] Compared with Li⁺, large-radius K⁺ ion is easy to cause deformation of electrode material, which seriously affects the recycling of battery. Guo et al. synthesized an electrode material SQ@MA with high potassium storage by simultaneously embedding Sb SAs and Sb quantum dots (QDs) into 3D Ti-based MXene aerogel (Figure 16g,h).^[59] Among them, the high load of Sb QDs ensured the storage of K⁺, and Sb SAs accelerated the charge-transfer dynamics between Sb QDs and MXene. Meanwhile, the porous structure of aerogel provided a fast electron transport path and stable structure, prolonging the battery life. As the anode, SQ@MA provided a high reversible capacity (521 mA h g⁻¹ at 0.1 A g⁻¹) and high capacity retention (94% at 1 A g⁻¹ even after 1000 cycles) (Figure 16i,j).

Due to the dendrite growth of the Li anode and the slow kinetics of the S cathode, Li-S batteries face the problems of low coulomb efficiency and poor electrochemical reversibility even if they have high energy density. Gu et al. replaced part of Ti atoms

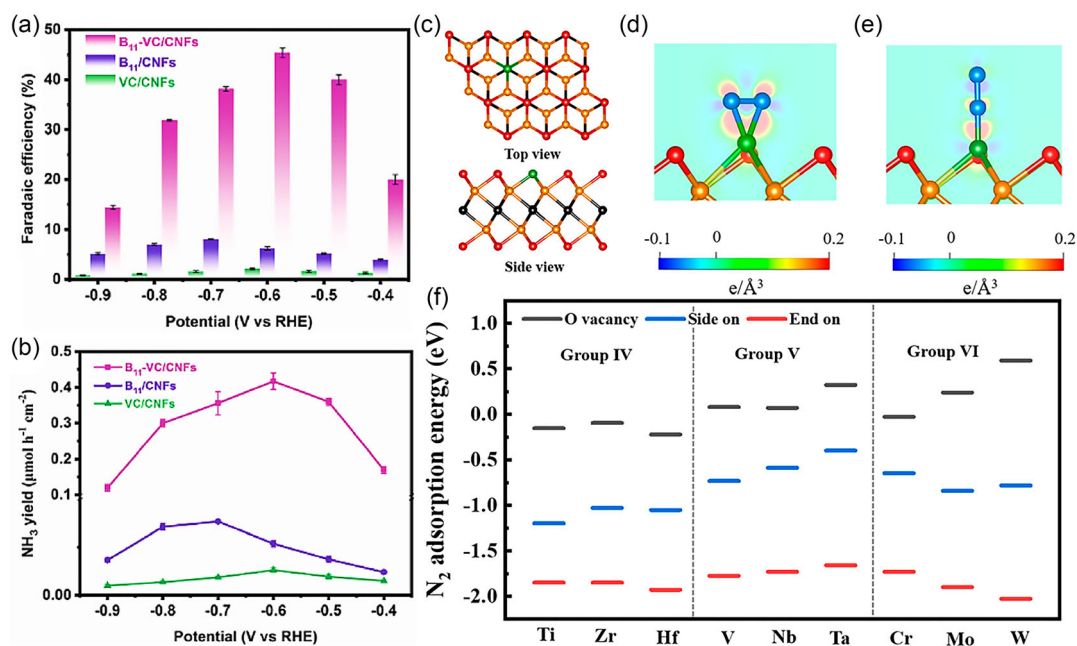


Figure 14. Comparison in a) FEs and b) NH₃ yields of B₁₁-VC/CNFs, VC/CNFs, and B₁₁/CNFs in N₂-saturated 0.5 M K₂SO₄. Reproduced with permission.^[70] Copyright 2021 Wiley-VCH GmbH. c) Top and side views of the structure of B-doped MXene. Charge density difference of N₂ adsorption on B-doped Mo₂CO₂ via d) side-on and e) end-on patterns (metal: orange, carbon: black, oxygen: red, boron: green, nitrogen: blue). f) Adsorption energies of N₂ on O vacancies and B centers for different MXenes. Reproduced with permission.^[90] Copyright 2019, American Chemical Society.

in Ti₃C₂Cl_x with 0.87 at% Zn, which effectively inhibited the dendrite of Li.^[107] Since Li can form an alloying phase with Zn, Li tended to nucleate uniformly on the surface of the Zn-Ti₃C₂Cl_x layer, and then grew further vertically at the nucleation sites due to a strong lightning rod effect at the edges, thus providing bowl-shaped lithium rather than lithium dendrites (Figure 17a). The electrode life of lithium anode with Zn-Ti₃C₂Cl_x membrane was greatly extended (1200 h), which was attributed to controlled Li nucleus growth. The performance of S cathode can also be improved by the Zn single atom on MXene. Zn-MXene was used as the main body of sulfur cathode, showing high reversible capacity (1136 mAh g⁻¹ at 0.2 C), high area capacity (5.3 mAh cm⁻² at 6 C), and high rate capacity (640 mAh g⁻¹).^[108] Due to the electron-donating ability of Zn, the single-atom Zn had a strong affinity with polysulfide, which was conducive to the adsorption and nucleation of polysulfide. In addition, the injection of Zn increased the valence band energy level of MXene, and reduced the rate-limiting reaction barrier from 0.91 to 0.71 eV, accelerating the redox kinetics of polysulfides.

In addition to serving as the main electrode, the diaphragm in battery play an important role in reducing the dendrite crystallization of the Li anode and avoiding the harm caused by the diffusion of polysulfide.^[109] Zhou et al. anchored Pt in In₂S₃/Ti₃C₂ compound by photochemical reduction method for the modification of polypropylene (PP) diaphragm of lithium-sulfur battery (Figure 17b,c).^[62] When 0.43 mg cm⁻² Pt-In₂S₃/Ti₃C₂ was supported on the PP film, 8.94 μm film was formed, which completely covered the void on the PP film and inhibited the migration of hydrogen polysulfide, but did not affect the diffusion of Li⁺. In addition, the modification of Pt SAC on PP film

not only promoted the adsorption of polysulfide and the oxidation of Li₂S on the sulfur cathode, but also regulated the uniform distribution of Li and inhibited the dendrite growth on the Li anode. The initial cell capacity of the cell equipped with modified PP film was improved, the coulomb efficiency was close to 100%, and the capacity attenuation per cycle was only 0.019%. Briefly, MXene modified by single atoms has a promising application prospect in battery system, including cathode, anode, and diaphragm.

Metal-air batteries, with air as the part of cathode, have an uninterrupted cathode active substance to provide energy in theory. The common air batteries are Li-O₂ battery and zinc air battery, in which oxygen participates in the reaction of cathode, and OER and ORR occur in the process of charging and discharging, respectively. Hence, rapid kinetics of OER/ORR and cycle stability are essential for metal-air batteries. Due to the unsaturated ligand of surface TM atoms, MXene QDs displayed good performance in Li-O₂ batteries, with high selectivity, significant charge/discharge potential (0.62 V), and good stability (240 cycles at 200 mA g⁻¹).^[110] Single-atom Se doped to Ti₃C₂ via a thermal reaction strategy, which was a high-performance Li cathode in Li-O₂ battery.^[45] Furthermore, the active center Se single atom was favorable to the adsorption and nucleation of LiO₂, and then promoted the charge transfer between the discharge products of Li₂O₂, resulting in the accelerated redox reaction. Li-O₂ battery assembled with SeSA-Ti₃C₂ as cathode had extremely high discharge capacity (17 260 mAh g⁻¹ at 100 mA g⁻¹). In addition, the single-atom Pt-doped heterojunction NBF-ReS₂/MoC₂T_x was found to have bifunctional OER/ORR activity, stable charging, and discharging for 100 h as the anode of the zinc-air battery.^[68]

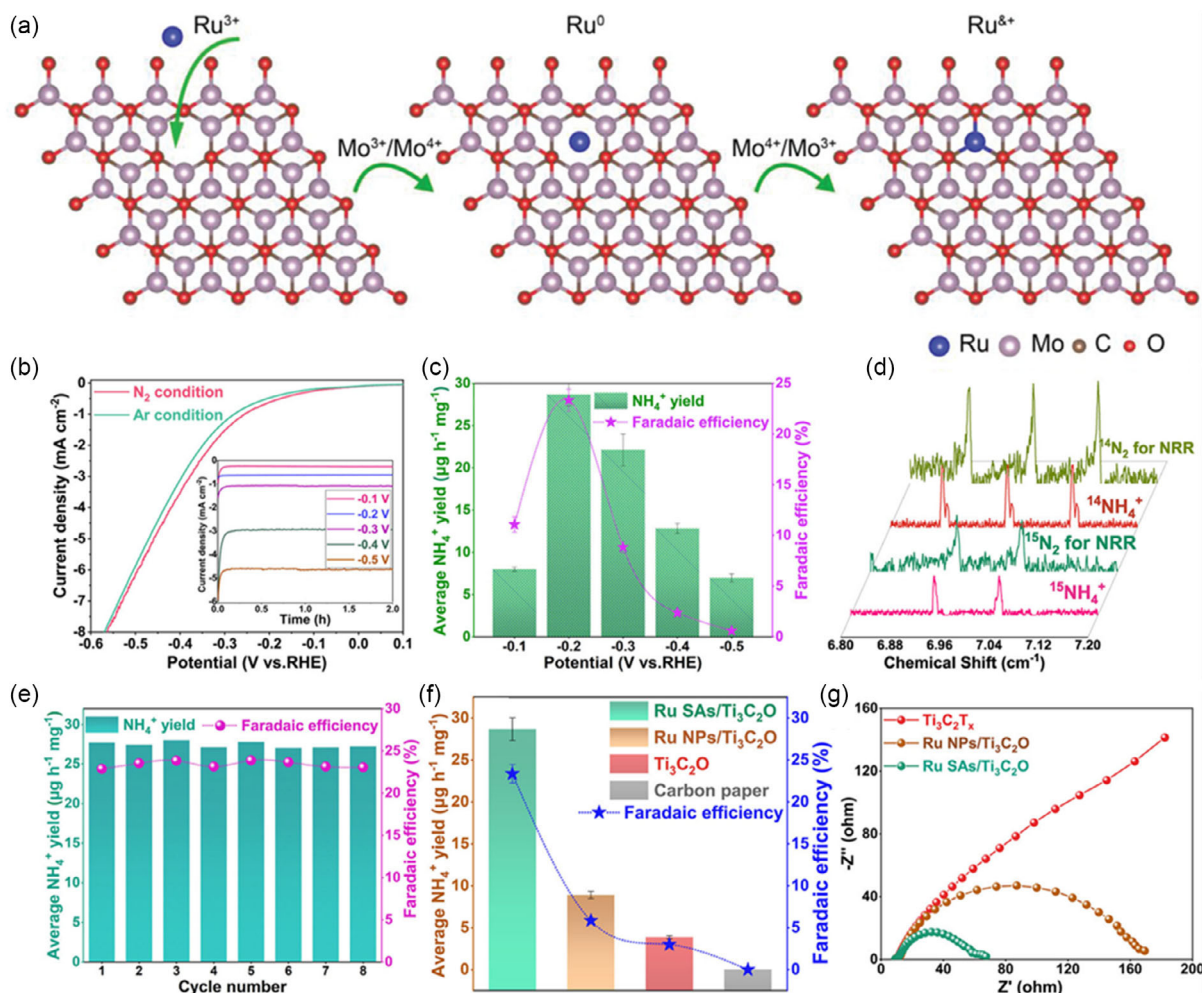


Figure 15. a) The fabrication mechanism of SA Ru–Mo₂CT_x. Reproduced with permission.^[64] Copyright 2020, Wiley-VCH GmbH. b) LSV curves of Ru SAs/Ti₃C₂O in 0.1 M HCl. c) NH₄⁺ yield and FE of Ru SAs/Ti₃C₂O. d) Isotopic labeling results of both ¹⁴NH₄⁺ and ¹⁵NH₄⁺ obtained from the nitrogen reduction reaction (NRR). e) Cycling stability of Ru SAs/Ti₃C₂O. f) NH₄⁺ yield and FE, and g) Nyquist plots of Ru SAs/Ti₃C₂O, Ru NPs/Ti₃C₂O, and Ti₃C₂O. Reproduced with permission.^[37] Copyright 2021, Wiley-VCH GmbH.

Moreover, in Li–CO₂ batteries, where bifunctional carbon dioxide reduction (CRR) and carbon evolution reaction (CER) electrodes are required, SA-modified MXenes demonstrate potential applications. Shi et al. screened bifunctional CRR/CER catalytic activity of TM-modified Mo₂CO₂, and found that Zn-, Mn-, Fe-, Ag-, and Cd-doped MXenes were prospective to be used in the cathode of Li–CO₂ batteries.^[111]

Supercapacitors are another type of energy-storage devices, which store energy through charge accumulation and reversible redox reactions. Compared with batteries, supercapacitors have a faster charge and discharge rate but a faster decay of energy density.^[112] Li et al. inserted Al ions into Ti₃C₂T_x, providing a specific capacity of 175 F g^{−1}, and due to the increased layer spacing, more Li ions were stored for subsequent ion exchange.^[113] V₃CrC₃T_x was synthesized by replacing part of the V atoms with Cr atoms, which increased the adsorption capacity for Zn ion.^[57] The synthesized Zn anode material based on V₃CrC₃T_x presented increased capacitance and discharge potential, with high surface energy density (51.12 mWh cm^{−2}) and foldability

(80.2% capacitance retention after 10 000 cycles), indicating high competitiveness in the use of flexible portable power supplies.

5.3. Applications in Sensors

5.3.1. Gas Sensors

Applications of MXenes in gas sensors have been reported including theoretical calculations and experiments. As a raw material for many industrial productions, NH₃ is one of the common industrial pollutions and is harmful for the environment and human body, thus there is an urgent need for fast and convenient NH₃ sensor. Single-layer Ti₃C₂ was synthesized by NaF + HCl etching without the addition of any single atom for the detection of NH₃ at room temperature.^[114] Not only NH₃, single-layer Ti₃C₂ also responded to other seven gases (CH₄, H₂S, H₂O, etc.), but had the highest selectivity for NH₃, which was four times more responsive than the next highest. However, both the multilayer Ti₃C₂ and the addition of

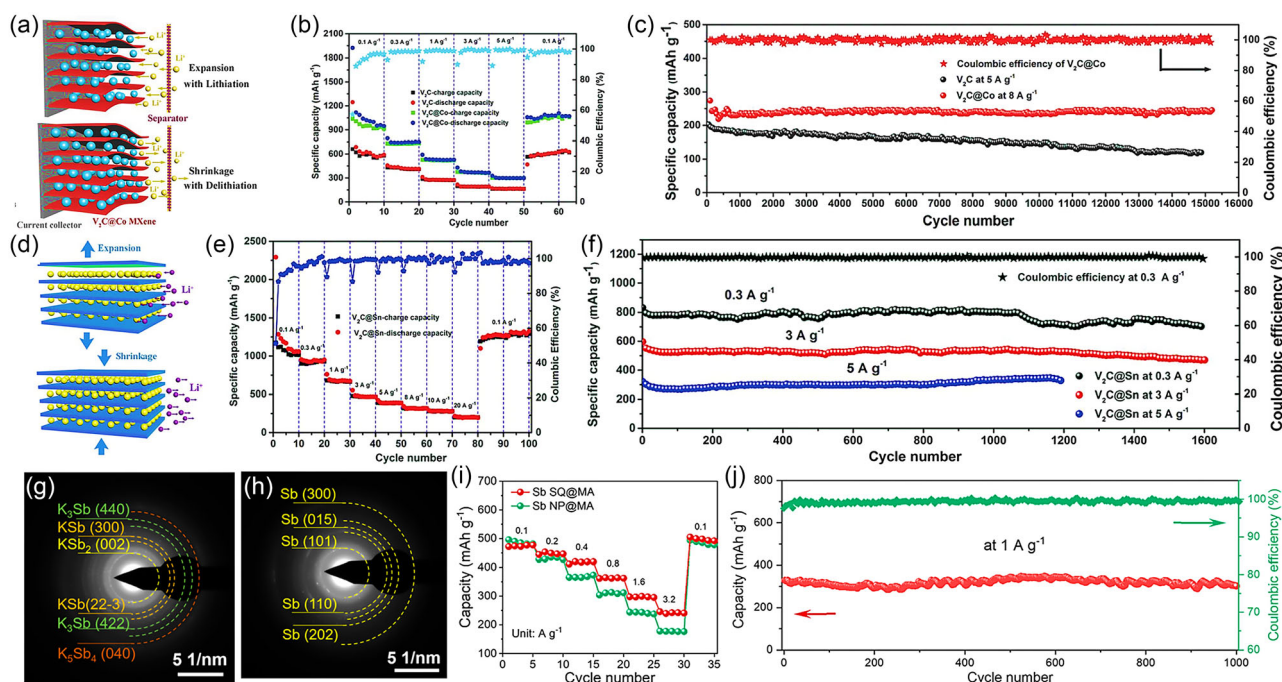


Figure 16. Schematic of expansion and shrinkage for a) V₂C@Co MXene d) and V₂C@Sn MXene. b,e) Rate performance. c,f) Long-term cycling performance. Reproduced with permission.^[56] Copyright 2018, Wiley-VCH GmbH. (d–f) Reproduced with permission.^[106] Copyright 2018, Wiley-VCH GmbH. Selected area electron diffraction patterns of the Sb SQ@MA electrode at g) fully discharged and h) charged states. i) Rate performance of Sb SQ@MA electrode. j) Long-term cycling performance of the Sb SQ@MA. Reproduced with permission.^[59] Copyright 2022, American Chemical Society.

metallic SA sites exhibited higher response to NH₃ than single-layer Ti₃C₂. Wu et al. fixed Ag onto the surface of oxygen-rich Ti₃C₂T_x via a self-reduction method, and tested the NH₃ sensor preformation of in dry and wet nitrogen, respectively.^[115] At the humidity of 40% relative humidity, the response sensitivity of Ag–Ti₃C₂ to NH₃ was the highest, which was attributed to the affinity between intercalated water and NH₃. However, excessive water would hinder the adsorption of NH₃ at the active site. With the conspicuously strong adsorption capacity for NH₃, Ag nanoparticles first adsorbed NH₃ and then the adsorbed NH₃ diffused to Ti₃C₂T_x, increasing the response resistance (Figure 18a–d). Triethylamine (TEA) has a strong smell of ammonia and is toxic to human body, which is urgent to be detected with a high sensitivity sensor. Zong et al. injected Pt single atoms into Ti₃C₂T_x, greatly improving the sensitivity and selectivity of Ti₃C₂T_x for TEA detection (Figure 18e,f).^[116] Theoretical calculations indicated that the reduced detection limit (14 ppb) was due to the chemical sensitization of Pt atom and the strong adsorption between Pt and TEA. Through NiCl molten salt etching, a NO₂ sensor Ni₁/TiCo_{0.5}N_{0.5} was synthesized with a low detection limit (190 ppb).^[117] Since MXene is easily oxidized in wet environments, more efforts are needed to obtain MXene-based SA sensors with better performance.

5.3.2. Biological Sensors

Photoelectrochemical (PEC) response is a new technique used for the detection and analysis of gases and organic compounds by amplifying photocurrent signals. Light capture ability and

interface redox reaction are the key to signal amplification. SACs as excellent biosensing catalysts have the active sites with the same coordination structure, corresponding to the unique enzyme active sites, and unique SA electron cloud distribution, which is conducive to signal recognition and amplification. In addition, 2D MXenes in combination with SACs with large interface, excellent conductivity, and easily adjustable electronic structure, have been investigated for biosensing systems. Qin et al. added single-Fe atoms to heterojunction of MXene and cuprous oxide to accelerate the interfacial redox reaction of P-type semiconductors.^[118] The introduction of Fe–N₄ site changed the adsorption of oxygen reduction intermediates on Cu₂O. In addition, the insoluble enzyme precipitation induced by Fe SACs inhibited PEC signal, suggesting that peroxidase could be detected by Fe SACs (Figure 19a). Furthermore, the addition of acetylcholinesterase regulated the enzyme activity of Fe and amplified the photoelectric signal, resulting in a low detection limit (0.08 ng mL⁻¹) and a wide linear range (0.5 ≈ 600 ng mL⁻¹) for organophosphorus pesticides.

Moreover, SACs on MXenes show promising applications in cancer diagnosis. Through calcinations, single-gold atoms were embedded in the Ti vacant of MXene, redistributing the charge of MXene through metal–carrier interactions (Figure 19b,c).^[119] At the SA Au sites, hydrogen peroxide obtained electrons and converted to hydroxyl radicals, resulting in the significant increase of electrochemical luminescence intensity, which was twice that of Au_{NPs}–MXene. In addition, in the synthesis process, part of Ti would be oxidized into TiO₂, and the heterojunction of MXene and TiO₂ was constructed, which accelerated the formation of

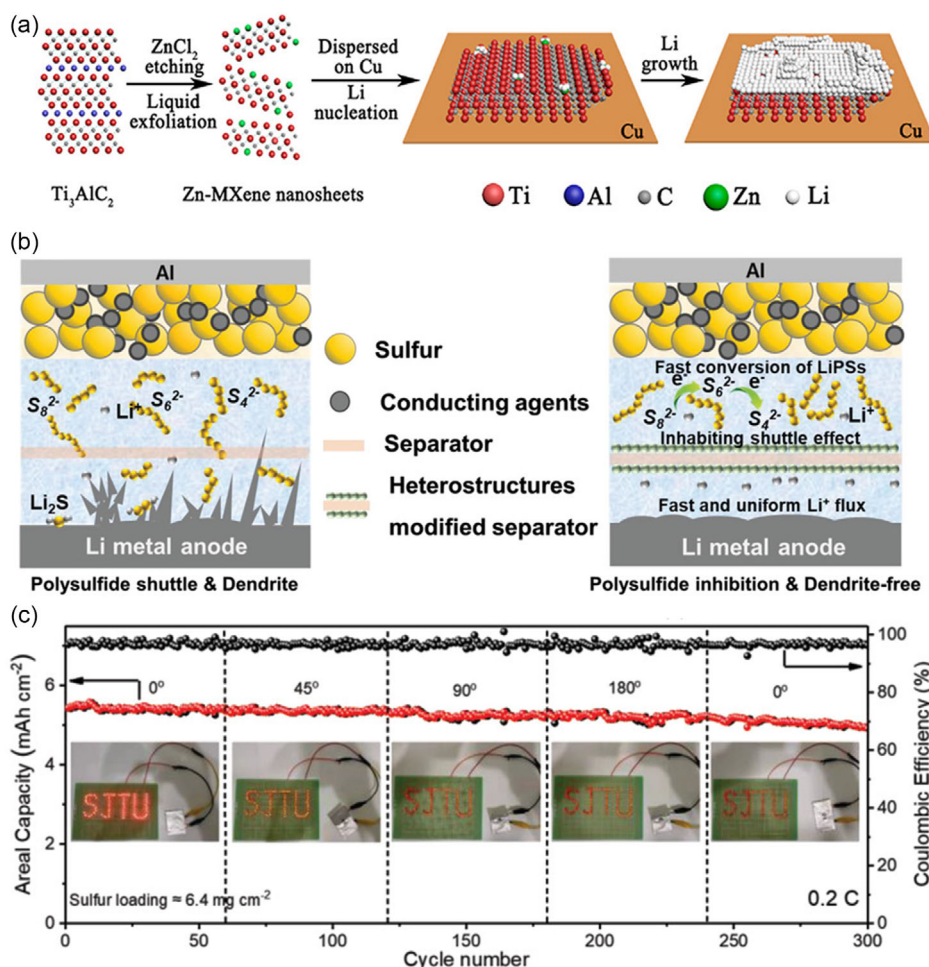


Figure 17. a) Synthesis process of Zn atoms immobilized on MXene layers (Zn-MXene) for the Li nucleation and growth. Reproduced with permission.^[107] Copyright 2020, American Chemical Society. b) Schematic illustrations of polysulfides suppressing and Li anode deposition process on PP and heterostructure-modified PP separator. c) Cycling performance of the Li–S battery with a Pt SAs/In₂S₃/Ti₃C₂@PP separator at different folding angles. Reproduced with permission.^[62] Copyright 2022, Wiley-VCH GmbH.

free radicals and facilitated the generation of electrochemical signals. For the clinical detection of miRNA-187 in triple negative breast cancer tumor tissue, the luminescence intensity was positively correlated with the concentration of miRNA-187.

6. Summary and Outlook

SACs combine the advantages of heterogeneous and homogeneous catalysts and show great potential in various fields. MXenes show promising prospects as substrates for SACs. In this review, we discuss the favorable properties of MXenes as carriers of single-metal sites, including abundant anchorage sites, adjustable electronic structure, and so on. Additionally, the characterization techniques of single atoms are summarized, including direct electron microscope images and indirect spectral analysis. Moreover, three strategies for fixing isolated metal sites on MXenes are condensed, including adsorption on the surface by bonding with functional groups, filling in M vacancies

and filling in T vacancies. We not only analyze the feasibility of the strategy by the stability and aggregation trend of single atoms at the anchorage sites, but also summarize the existing experimental studies on the successful synthesis of single-atom sites on MXenes. The synthesis of single atoms on MXenes by different methods involves the following three steps: 1) metal cations approach MXene under the drive of electrostatic attraction or high surface energy; 2) the metal cations are reduced to zero valence by the reducibility of MXene itself or additional reductants; and 3) the metal is oxidized to a high valence state through generating significant electron transfer with MXene. For surface adsorption strategies, single atoms have high surface energy and readily available heteroatomic modifications that allow for more possibilities in their electronic structures. For the vacancy filling strategy, isolated atoms enter the MXene lattice, which means better anchoring effect. However, to ensure the stability of the structure, the types and loads of TM atoms are limited.

The catalytic activity of SACs is closely related to their coordination structure, and the advanced characterization techniques

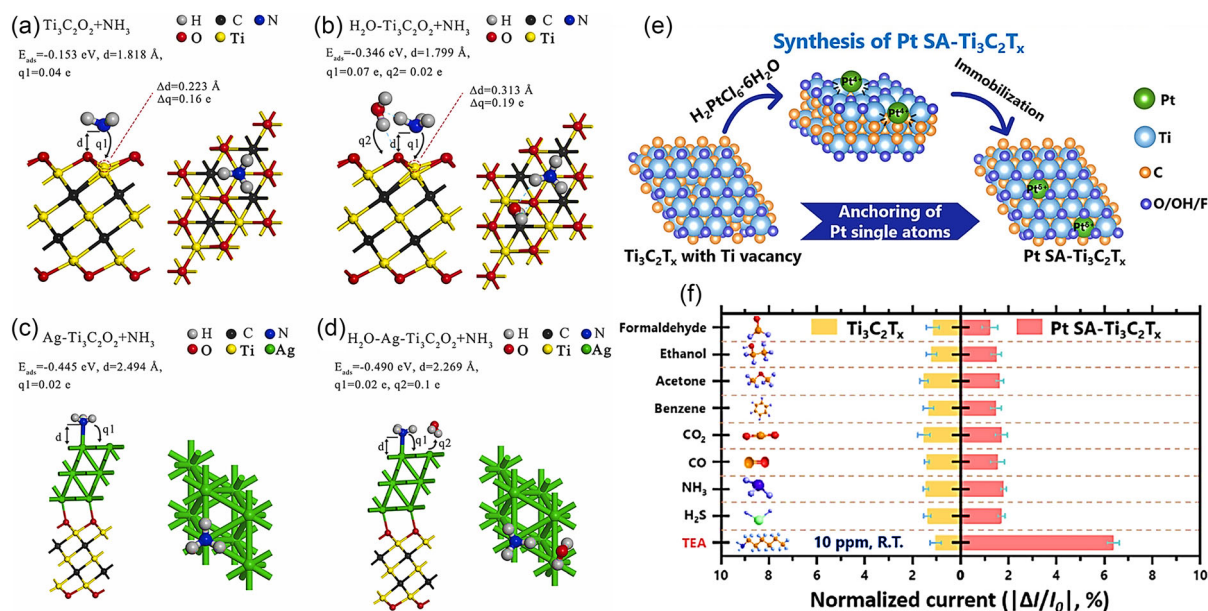


Figure 18. Side view (left) and top view (right) of minimum energy configurations for NH₃ adsorbed on a) Ti₃C₂O₂, b) Ti₃C₂O₂ with pre-adsorbed H₂O, c) Ag-Ti₃C₂O₂, and d) Ag-Ti₃C₂O₂ with pre-adsorbed H₂O. Reproduced with permission.^[115] Copyright 2022, Elsevier. e) Schematic diagram of the synthesis of Pt SA-Ti₃C₂T_x. f) High specificity of the sensors toward triethylamine (TEA) compared with other volatile organic compounds and reducing gases. Reproduced with permission.^[116] Copyright 2022, American Chemical Society.

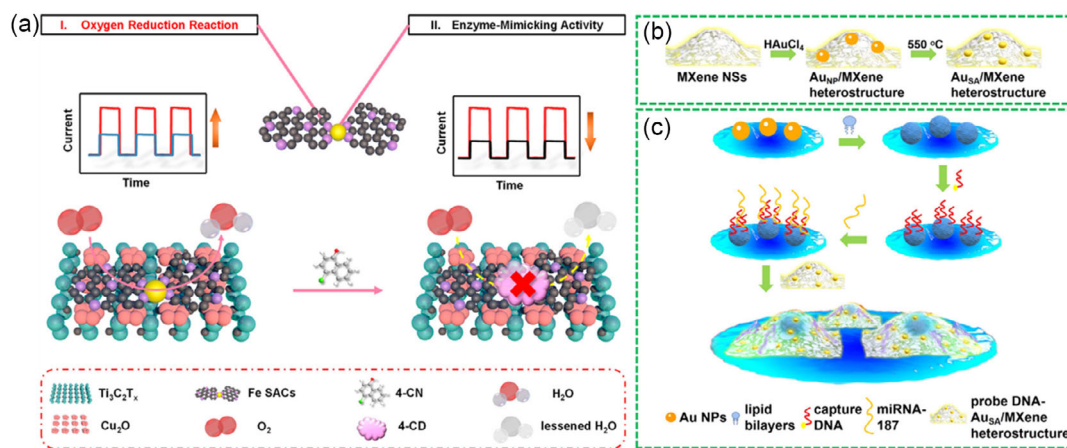


Figure 19. a) Operation of Fe SACs/Cu₂O/Ti₃C₂T_x-based photoelectrochemical (PEC) analytical platform. Reproduced with permission.^[118] Copyright 2022, American Chemical Society. b) Fabrication of the Au₅₅A/MXene and c) Electrochemiluminescence sensing system based on the Au₅₅A/MXene and fluid nanoislands for detecting miRNA-187. Reproduced with permission.^[119] Copyright 2022, American Chemical Society.

make them possible to understand the coordination number and coordination atom of single atoms on MXenes. Through in situ characterization, the catalytic mechanism of SA sites in the catalytic process can be further analyzed. Moreover, the combination of the theoretical calculation and experiment is efficient means for improving the performance of SACs, especially the known atomic structure of MXene and controllable coordination sites are advantageous to the construction of calculation model. However, even the structures of SA active sites with high catalytic activity have been successfully screened by theoretical calculations; it is still challenging to synthesize these sites with specified coordination structure on MXene by experimental means.

Therefore, to obtain excellent-performance SACs supported by MXenes, it is necessary to further understand the structure–activity relationship between coordination environment and catalytic performance by in situ characterization. In addition, combining experiments with theoretical calculations could facilitate in depth understanding of the reaction mechanisms.

The applications of MXene-based SACs in electrocatalysis, energy storage, and sensors are summarized. The tunability of M, X, and T elements in MXene is conducive to the regulation of electronic structure, which can improve the adsorption and desorption behavior of reaction intermediates at single-atom sites and reduce the electrocatalytic reaction barrier.

For energy-storage devices, MXene-based SACs play an active role in the cathode, anode, and electrolyte diaphragm in advanced battery systems, which accelerate the reaction kinetics of the cathode, inhibit the dendrite precipitation of the metal anode, while avoiding adverse diffusion from the cathode to the anode. However, improvements in battery performance, including ion storage and cyclic stability, are limited only by the single-atomic sites due to the instability. Constructing additional MXene-based heterojunctions is usually necessary, where the single-metal atoms are further stabilized. MXene-based SACs show high responsiveness and selectivity to specific gases or organic compounds, but due to their easily oxidized properties, more efforts are needed for their detection applications in humid environments. Additionally, the application prospects of MXene-based SACs can be extended to more other fields, which could be studied by the combination of theoretical calculation and experimental verification.

Acknowledgements

This work was supported by the National Natural Science Foundation of China (No. 22075099), the Natural Science Foundation of Jilin Province (No. 202201010511C), and the Education Department of Jilin Province (No. JJKH20220967K).

Conflict of Interest

The authors declare no conflict of interest.

Keywords

batteries, electrocatalyses, MXenes, sensors, single-atom catalysts

Received: November 15, 2022

Revised: January 8, 2023

Published online: January 27, 2023

- [1] B. Qiao, A. Wang, X. Yang, L. F. Allard, Z. Jiang, Y. Cui, J. Liu, J. Li, T. Zhang, *Nat. Chem.* **2011**, *3*, 634.
- [2] H. Yang, R. Shi, L. Shang, T. Zhang, *Small Struct.* **2021**, *2*, 2100007.
- [3] Y. Shi, Z. R. Ma, Y. Y. Xiao, Y. C. Yin, W. M. Huang, Z. C. Huang, Y. Z. Zheng, F. Y. Mu, R. Huang, G. Y. Shi, Y. Y. Sun, X. H. Xia, W. Chen, *Nat. Commun.* **2021**, *12*, 3021.
- [4] T. Tang, Z. Wang, J. Guan, *Acta Phys. Chim. Sin.* **2023**, *39*, 2208033.
- [5] Z. Li, B. Li, Y. Hu, X. Liao, H. Yu, C. Yu, *Small Struct.* **2022**, *3*, 2200041.
- [6] Y. Ren, Y. Tang, L. Zhang, X. Liu, L. Li, S. Miao, D. Sheng Su, A. Wang, J. Li, T. Zhang, *Nat. Commun.* **2019**, *10*, 4500.
- [7] S. Ren, B. Ye, S. Li, L. Pang, Y. Pan, H. Tang, *Nano Res.* **2022**, *15*, 1500.
- [8] X. Bai, L. Wang, B. Nan, T. Tang, X. Niu, J. Guan, *Nano Res.* **2022**, *15*, 6019.
- [9] J. Guan, X. Bai, T. Tang, *Nano Res.* **2022**, *15*, 818.
- [10] Q. Zhang, J. Guan, *Nano Res.* **2022**, *15*, 38.
- [11] X. Bai, Z. Duan, B. Nan, L. Wang, T. Tang, J. Guan, *Chin. J. Catal.* **2022**, *43*, 2240.
- [12] J. Han, M. Zhang, X. Bai, Z. Duan, T. Tang, J. Guan, *Inorg. Chem. Front.* **2022**, *9*, 3559.
- [13] N. Liu, Z. Duan, Q. Zhang, J. Guan, *Chem. Eng. J.* **2021**, *419*, 129567.
- [14] T. Tang, S. Li, J. Sun, Z. Wang, J. Guan, *Nano Res.* **2022**, *15*, 8714.
- [15] S. Li, J. Sun, J. Guan, *Chin. J. Catal.* **2021**, *42*, 511.
- [16] M. Naguib, M. Kurtoglu, V. Presser, J. Lu, J. Niu, M. Heon, L. Hultman, Y. Gogotsi, M. W. Barsoum, *Adv. Mater.* **2011**, *23*, 4248.
- [17] M. Ghidui, M. Naguib, C. Shi, O. Mashtalir, L. M. Pan, B. Zhang, J. Yang, Y. Gogotsi, S. J. Billinge, M. W. Barsoum, *Chem. Commun. (Camb.)* **2014**, *50*, 9517.
- [18] B. Jiang, T. Yang, T. Wang, C. Chen, M. Yang, X. Yang, J. Zhang, Z. Kou, *Chem. Eng. J.* **2022**, *442*, 136119.
- [19] S. Yang, P. Zhang, F. Wang, A. G. Ricciardulli, M. R. Lohe, P. W. M. Blom, X. Feng, *Angew. Chem. Int. Ed.* **2018**, *57*, 15491.
- [20] M. Li, J. Lu, K. Luo, Y. Li, K. Chang, K. Chen, J. Zhou, J. Rosen, L. Hultman, P. Eklund, P. O.Å. Persson, S. Du, Z. Chai, Z. Huang, Q. Huang, *J. Am. Chem. Soc.* **2019**, *141*, 4730.
- [21] T. Li, L. Yao, Q. Liu, J. Gu, R. Luo, J. Li, X. Yan, W. Wang, P. Liu, B. Chen, W. Zhang, W. Abbas, R. Naz, D. Zhang, *Angew. Chem. Int. Ed. Engl.* **2018**, *57*, 6115.
- [22] L.-Y. Xiu, Z.-Y. Wang, J.-S. Qiu, *Rare Met.* **2020**, *39*, 1237.
- [23] Z. Leong, H. Jin, Z. M. Wong, K. Nemani, B. Anasori, T. L. Tan, *Chem. Mater.* **2022**, *34*, 9062.
- [24] X. Bai, J. Guan, *Chin. J. Catal.* **2022**, *43*, 2057.
- [25] C. Cheng, X. Zhang, M. Wang, S. Wang, Z. Yang, *Phys. Chem. Chem. Phys.* **2018**, *20*, 3504.
- [26] Q. Zhang, J. Guan, *Energy Environ. Mater.* **2021**, *4*, 307.
- [27] C.-Y. Liu, E. Y. Li, *ACS Appl. Mater. Interfaces* **2019**, *11*, 1638.
- [28] M. Li, Y. Wang, T. Li, J. Li, L. Huang, Q. Liu, J. Gu, D. Zhang, *J. Mater. Chem. A* **2021**, *9*, 922.
- [29] S. Li, P. Tuo, J. Xie, X. Zhang, J. Xu, J. Bao, B. Pan, Y. Xie, *Nano Energy* **2018**, *47*, 512.
- [30] T. Tang, Z. Wang, J. Guan, *Chin. J. Catal.* **2022**, *43*, 636.
- [31] J. Han, J. Guan, *Chin. J. Catal.* **2023**, *44*, 1.
- [32] J. Yang, W. Li, D. Wang, Y. Li, *Small Struct.* **2021**, *2*, 2000051.
- [33] Y. Gao, Y. Cao, Y. Gu, H. Zhuo, G. Zhuang, S. Deng, X. Zhong, Z. Wei, J. Chen, X. Pan, J.-g. Wang, *Appl. Surf. Sci.* **2019**, *465*, 911.
- [34] H. Oschinski, Á. Morales-García, F. Illas, *J. Phys. Chem. C* **2021**, *125*, 2477.
- [35] M. Keyhanian, D. Farmanzadeh, Á. Morales-Garcia, F. Illas, *J. Mater. Chem. A* **2022**, *10*, 8846.
- [36] Y.-H. Chen, M.-Y. Qi, Y.-H. Li, Z.-R. Tang, T. Wang, J. Gong, Y.-J. Xu, *Cell Rep. Phys. Sci.* **2021**, *2*, 100371.
- [37] G. Chen, M. Ding, K. Zhang, Z. Shen, Y. Wang, J. Ma, A. Wang, Y. Li, H. Xu, *ChemSusChem* **2022**, *15*, e202102352.
- [38] X. Peng, Y. Mi, X. Liu, J. Sun, Y. Qiu, S. Zhang, X. Ke, X. Wang, J. Luo, *J. Mater. Chem. A* **2022**, *10*, 6134.
- [39] L. Dai, Y. Shen, J. Z. Chen, L. Zhou, X. Wu, Z. Li, J. Wang, W. Huang, J. T. Miller, Q. Wang, A. Cao, Y. Wu, *Small* **2022**, *18*, 2105226.
- [40] Q. Zhao, C. Zhang, R. Hu, Z. Du, J. Gu, Y. Cui, X. Chen, W. Xu, Z. Cheng, S. Li, B. Li, Y. Liu, W. Chen, C. Liu, J. Shang, L. Song, S. Yang, *ACS Nano* **2021**, *15*, 4927.
- [41] H. Liu, Z. Hu, Q. Liu, P. Sun, Y. Wang, S. Chou, Z. Hu, Z. Zhang, *J. Mater. Chem. A* **2020**, *8*, 24710.
- [42] D. Zhao, Z. Chen, W. Yang, S. Liu, X. Zhang, Y. Yu, W. C. Cheong, L. Zheng, F. Ren, G. Ying, X. Cao, D. Wang, Q. Peng, G. Wang, C. Chen, *J. Am. Chem. Soc.* **2019**, *141*, 4086.
- [43] S. Park, Y.-L. Lee, Y. Yoon, S. Y. Park, S. Yim, W. Song, S. Myung, K.-S. Lee, H. Chang, S. S. Lee, K.-S. An, *Appl. Catal., B* **2022**, *304*, 120989.
- [44] S. Zhou, Y. Zhao, R. Shi, Y. Wang, A. Ashok, F. Heraly, T. Zhang, J. Yuan, *Adv. Mater.* **2022**, *34*, 2204388.
- [45] D. Zhao, P. Wang, H. Di, P. Zhang, X. Hui, L. Yin, *Adv. Funct. Mater.* **2021**, *31*, 2010544.
- [46] D. A. Kuznetsov, Z. Chen, P. V. Kumar, A. Tsoukalou, A. Kierzkowska, P. M. Abdala, O. V. Safonova, A. Fedorov, C. R. Muller, *J. Am. Chem. Soc.* **2019**, *141*, 17809.

- [47] D. A. Kuznetsov, Z. Chen, P. M. Abdala, O. V. Safonova, A. Fedorov, C. R. Muller, *J. Am. Chem. Soc.* **2021**, *143*, 5771.
- [48] N. Li, X. Chen, W. J. Ong, D. R. MacFarlane, X. Zhao, A. K. Cheetham, C. Sun, *ACS Nano* **2017**, *11*, 10825.
- [49] C. Cheng, X. Zhang, Z. Yang, K. Hermansson, *Adv. Theory Simul.* **2019**, *2*, 1900006.
- [50] H. Bao, Y. Qiu, X. Peng, J. A. Wang, Y. Mi, S. Zhao, X. Liu, Y. Liu, R. Cao, L. Zhuo, J. Ren, J. Sun, J. Luo, X. Sun, *Nat. Commun.* **2021**, *12*, 238.
- [51] X. Zhao, X. Zheng, Q. Lu, Y. Li, F. Xiao, B. Tang, S. Wang, D. Y. W. Yu, A. L. Rogach, *EcoMat* **2022**, *5*, e12293.
- [52] J. Zhang, E. Wang, S. Cui, S. Yang, X. Zou, Y. Gong, *Nano Lett.* **2022**, *22*, 1398.
- [53] V. Ramalingam, P. Varadhan, H. C. Fu, H. Kim, D. Zhang, S. Chen, L. Song, D. Ma, Y. Wang, H. N. Alshareef, J. H. He, *Adv. Mater.* **2019**, *31*, 1903841.
- [54] Y. Zou, S. A. Kazemi, G. Shi, J. Liu, Y. Yang, N. M. Bedford, K. Fan, Y. Xu, H. Fu, M. Dong, M. Al-Mamun, Y. L. Zhong, H. Yin, Y. Wang, P. Liu, H. Zhao, *EcoMat* **2023**, *5*, e12274.
- [55] W. Peng, J. Han, Y. R. Lu, M. Luo, T. S. Chan, M. Peng, Y. Tan, *ACS Nano* **2022**, *16*, 4116.
- [56] C. Wang, H. Xie, S. Chen, B. Ge, D. Liu, C. Wu, W. Xu, W. Chu, G. Babu, P. M. Ajayan, L. Song, *Adv. Mater.* **2018**, *30*, 1802525.
- [57] H. Wang, Y. Xue, X. Song, S. Lei, H. Yu, C.-F. Du, Z. Ren, R. Guo, F. Zhou, *J. Mater. Chem. A* **2022**, *10*, 20953.
- [58] W. Lin, Y.-R. Lu, W. Peng, M. Luo, T.-S. Chan, Y. Tan, *J. Mater. Chem. A* **2022**, *10*, 9878.
- [59] X. Guo, H. Gao, S. Wang, G. Yang, X. Zhang, J. Zhang, H. Liu, G. Wang, *Nano Lett.* **2022**, *22*, 1225.
- [60] L. Jin, S. You, Y. Yao, H. Chen, Y. Wang, Y. Liu, *J. Mater. Chem. A* **2021**, *9*, 25964.
- [61] S. Yang, J. Kim, Y. J. Tak, A. Soon, H. Lee, *Angew. Chem. Int. Ed. Engl.* **2016**, *55*, 2058.
- [62] C. Zhou, M. Li, N. Hu, J. Yang, H. Li, J. Yan, P. Lei, Y. Zhuang, S. Guo, *Adv. Funct. Mater.* **2022**, *32*, 2204635.
- [63] L. Jin, S. You, N. Ren, B. Ding, Y. Liu, *Environ. Sci. Technol.* **2022**, *56*, 11750.
- [64] W. Peng, M. Luo, X. Xu, K. Jiang, M. Peng, D. Chen, T. S. Chan, Y. Tan, *Adv. Energy Mater.* **2020**, *10*, 112658.
- [65] A. Djire, H. Zhang, B. J. Reinhart, O. C. Nwamba, N. R. Neale, *ACS Catal.* **2021**, *11*, 3128.
- [66] T. Tang, Z. Wang, J. Guan, *Adv. Funct. Mater.* **2022**, *32*, 2111504.
- [67] L. Xiao, Z. Wang, J. Guan, *Coord. Chem. Rev.* **2022**, *472*, 214777.
- [68] M. Yi, N. Li, B. Lu, L. Li, Z. Zhu, J. Zhang, *Energy Storage Mater.* **2021**, *42*, 418.
- [69] C. Cui, R. Cheng, H. Zhang, C. Zhang, Y. Ma, C. Shi, B. Fan, H. Wang, X. Wang, *Adv. Funct. Mater.* **2020**, *30*, 2000693.
- [70] Y. Wen, Z. Zhuang, H. Zhu, J. Hao, K. Chu, F. Lai, W. Zong, C. Wang, P. Ma, W. Dong, S. Lu, T. Liu, M. Du, *Adv. Energy Mater.* **2021**, *11*, 2102138.
- [71] J. Zhang, Y. Zhao, X. Guo, C. Chen, C.-L. Dong, R.-S. Liu, C.-P. Han, Y. Li, Y. Gogotsi, G. Wang, *Nat. Catal.* **2018**, *1*, 985.
- [72] Z. Kang, J. Cai, D. Ye, H. Zhao, J. Luo, J. Zhang, *Chem. Eng. J.* **2022**, *446*, 137443.
- [73] L. Kong, X. Liang, M. Wang, C.-M. L. Wu, *ACS Sustainable Chem. Eng.* **2022**, *10*, 4152.
- [74] Y. Zhu, G. Xu, W. Song, Y. Zhao, Z. He, Z. Miao, *Ceram. Int.* **2021**, *47*, 30005.
- [75] T. Tang, Z. Duan, D. Baimanov, X. Bai, X. Liu, L. Wang, Z. Wang, J. Guan, *Nano Res.* **2022**, <https://doi.org/10.1007/s12274-022-5001-3>.
- [76] J. Han, J. Guan, *Nano Res.* **2022**, <https://doi.org/10.1007/s12274-022-4874-7>.
- [77] C. Xu, C. Fan, X. Zhang, H. Chen, X. Liu, Z. Fu, R. Wang, T. Hong, J. Cheng, *ACS Appl. Mater. Interfaces* **2020**, *12*, 19539.
- [78] N. Ma, N. Li, T. Wang, X. Ma, J. Fan, *J. Mater. Chem. A* **2022**, *10*, 1390.
- [79] N. Ma, Y. Wang, Y. Zhang, B. Liang, J. Zhao, J. Fan, *Appl. Surf. Sci.* **2022**, *596*, 153574.
- [80] Y. Liu, X. Liu, Z. Lv, R. Liu, L. Li, J. Wang, W. Yang, X. Jiang, X. Feng, B. Wang, *Angew. Chem. Int. Ed. Engl.* **2022**, *61*, e202117617.
- [81] Z. Chen, X. Fan, Z. Shen, X. Ruan, L. Wang, H. Zeng, J. Wang, Y. An, Y. Hu, *ChemCatChem* **2020**, *12*, 4059.
- [82] Z. Kou, W. Zang, W. Pei, L. Zheng, S. Zhou, S. Zhang, L. Zhang, J. Wang, *J. Mater. Chem. A* **2020**, *8*, 3071.
- [83] D. Kan, R. Lian, D. Wang, X. Zhang, J. Xu, X. Gao, Y. Yu, G. Chen, Y. Wei, *J. Mater. Chem. A* **2020**, *8*, 17065.
- [84] D. Kan, D. Wang, X. Zhang, R. Lian, J. Xu, G. Chen, Y. Wei, *J. Mater. Chem. A* **2020**, *8*, 3097.
- [85] B. Wei, Z. Fu, D. Legut, T. C. Germann, S. Du, H. Zhang, J. S. Francisco, R. Zhang, *Adv. Mater.* **2021**, *33*, e2102595.
- [86] S. S. A. Shah, T. Najam, M. Wen, S.-Q. Zang, A. Waseem, H.-L. Jiang, *Small Struct.* **2022**, *3*, 2100090.
- [87] K. Eid, Q. Lu, S. Abdel-Azeim, A. Soliman, A. M. Abdullah, A. M. Abdelgwad, R. P. Forbes, K. I. Ozoemena, R. S. Varma, M. F. Shibli, *J. Mater. Chem. A* **2022**, *10*, 1965.
- [88] N. Li, J. Peng, Z. Shi, P. Zhang, X. Li, *Chin. J. Catal.* **2022**, *43*, 1906.
- [89] D. Qu, X. Peng, Y. Mi, H. Bao, S. Zhao, X. Liu, J. Luo, *Nanoscale* **2020**, *12*, 17191.
- [90] S. Zheng, S. Li, Z. Mei, Z. Hu, M. Chu, J. Liu, X. Chen, F. Pan, *J. Phys. Chem. Lett.* **2019**, *10*, 6984.
- [91] N. Zhang, M.-y. Wang, J.-Y. Liu, *Mol. Catal.* **2022**, *531*, 112658.
- [92] H. Li, S. Wei, H. Wang, Q. Cai, J. Zhao, *J. Colloid Interface Sci.* **2021**, *588*, 1.
- [93] X. Zhai, H. Dong, Y. Li, X. Yang, L. Li, J. Yang, Y. Zhang, J. Zhang, H. Yan, G. Ge, *J. Colloid Interface Sci.* **2022**, *605*, 897.
- [94] Y. Gao, H. Zhuo, Y. Cao, X. Sun, G. Zhuang, S. Deng, X. Zhong, Z. Wei, J. Wang, *Chin. J. Catal.* **2019**, *40*, 152.
- [95] B. Huang, N. Li, W.-J. Ong, N. Zhou, *J. Mater. Chem. A* **2019**, *7*, 27620.
- [96] H. Luo, X. Wang, C. Wan, L. Xie, M. Song, P. Qian, *Nanomaterials (Basel)* **2022**, *12*, 1081.
- [97] K. Niu, L. Chi, J. Rosen, J. Bjork, *J. Phys. Chem. Lett.* **2022**, *13*, 2800.
- [98] Y. Cheng, J. Dai, Y. Song, Y. Zhang, *Nanoscale* **2019**, *11*, 18132.
- [99] Q. Fang, Y. Gao, W. Zhang, F. Sun, J. Pan, G. Zhuang, S. Deng, Z. Yao, J. Wang, *J. Phys. Chem. C* **2021**, *125*, 14636.
- [100] Y. Luo, M. Li, Y. Dai, X. Zhang, R. Zhao, F. Jiang, C. Ling, Y. Huang, *J. Mater. Chem. A* **2021**, *9*, 15217.
- [101] B. Huang, J. Yang, G. Ren, Y. Qian, Y.-W. Zhang, *Appl. Catal., A Gen.* **2022**, *646*, 118886.
- [102] S. Tang, T. Liu, Q. Dang, X. Zhou, X. Li, T. Yang, Y. Luo, E. Sharman, J. Jiang, *J. Phys. Chem. Lett.* **2020**, *11*, 5051.
- [103] L. Li, X. Wang, H. Guo, G. Yao, H. Yu, Z. Tian, B. Li, L. Chen, *Small Methods* **2019**, *3*, 118886.
- [104] A. Saha, N. Shpigel, Rosy, N. Leifer, S. Taragin, T. Sharabani, H. Aviv, I. Perelshtein, G. D. Nessim, M. Noked, Y. Gogotsi, *Adv. Funct. Mater.* **2021**, *31*, 2106294.
- [105] L. Shen, Y.-W. Song, J. Wang, C.-X. Zhao, C.-X. Bi, S.-Y. Sun, X.-Q. Zhang, B.-Q. Li, Q. Zhang, *Small Struct.* **2022**, *n/a*, 2200205.
- [106] C. Wang, S. Chen, H. Xie, S. Wei, C. Wu, L. Song, *Adv. Energy Mater.* **2019**, *9*, 1802977.
- [107] J. Gu, Q. Zhu, Y. Shi, H. Chen, D. Zhang, Z. Du, S. Yang, *ACS Nano* **2020**, *14*, 891.
- [108] D. Zhang, S. Wang, R. Hu, J. Gu, Y. Cui, B. Li, W. Chen, C. Liu, J. Shang, S. Yang, *Adv. Funct. Mater.* **2020**, *30*, 2002471.
- [109] J. Tang, X. Peng, T. Lin, X. Huang, B. Luo, L. Wang, *eScience* **2021**, *1*, 203.

- [110] P. Wang, D. Zhao, X. Hui, Z. Qian, P. Zhang, Y. Ren, Y. Lin, Z. Zhang, L. Yin, *Adv. Energy Mater.* **2021**, *11*, 2003069.
- [111] Y. Shi, B. Wei, D. Legut, S. Du, J. S. Francisco, R. Zhang, *Adv. Funct. Mater.* **2022**, 2003069.
- [112] Y. Tian, M. Ju, Y. Luo, X. Bin, X. Lou, W. Que, *Chem. Eng. J.* **2022**, *446*, 137451.
- [113] Y. Li, Y. Deng, J. Zhang, Y. Han, W. Zhang, X. Yang, X. Zhang, W. Jiang, *Nanoscale* **2019**, *11*, 21981.
- [114] M. Wu, M. He, Q. Hu, Q. Wu, G. Sun, L. Xie, Z. Zhang, Z. Zhu, A. Zhou, *ACS Sens.* **2019**, *4*, 2763.
- [115] H. Wu, J. Yu, G. Yao, Z. Li, W. Zou, X. Li, H. Zhu, Z. Huang, Z. Tang, *Sens. Actuators, B* **2022**, *369*, 132195.
- [116] B. Zong, Q. Xu, S. Mao, *ACS Sens.* **2022**, *7*, 1874.
- [117] W. Chen, P. Li, J. Yu, P. Cui, X. Yu, W. Song, C. Cao, *Nano Res.* **2022**, *15*, 9544.
- [118] Y. Qin, J. Wen, X. Wang, L. Jiao, X. Wei, H. Wang, J. Li, M. Liu, L. Zheng, L. Hu, W. Gu, C. Zhu, *ACS Nano* **2022**, *16*, 2997.
- [119] Y. Nie, P. Wang, Q. Ma, X. Su, *Anal. Chem.* **2022**, *94*, 11016.
- [120] X. Wang, X. Shen, Y. Gao, Z. Wang, R. Yu, L. Chen, *J. Am. Chem. Soc.* **2015**, *137*, 2715.
- [121] J. Yang, A. Wang, S. Zhang, H. Wu, L. Chen, *Comput. Mater. Sci.* **2018**, *153*, 303.
- [122] P. Li, J. Zhu, A. D. Handoko, R. Zhang, H. Wang, D. Legut, X. Wen, Z. Fu, Z. W. Seh, Q. Zhang, *J. Mater. Chem. A* **2018**, *6*, 4271.



Xue Bai received her B.S. degree from Shaanxi Normal University in 2020. She is now a Ph.D. student in Jilin University under the supervision of Professor Jingqi Guan. Her research interests focus on the synthesis of single-atom catalysts and the development of 2D materials for electrocatalysis and energy storage.



Jingqi Guan is currently a professor of Chemistry, Jilin University. He received his B.S. and Ph.D. degrees in chemistry from Jilin University. He worked as a postdoctoral research fellow in the University of California at Berkeley from 2012 to 2013 and in the Dalian Institute of Chemical Physics from 2014 to 2018. His research interests are in engineering single-atom catalysts and 2D materials for catalysis, energy, and biosensors. He is on the Editorial Boards of *Chin. J. Catal.* and *Acta Phys.-Chim. Sin.* He has published more than 180 peer-reviewed papers.